THE EFFECTS OF INJECTION ANGLE ON THE STRUCTURE OF CHOKED GASEOUS JETS

By

ALEX MICHAEL SHERIDAN

Bachelor of Science in Mechanical Engineering

Oklahoma State University

Stillwater, Oklahoma

2012

Submitted to the Faculty of the
Graduate College of the
Oklahoma State University
in partial fulfillment of
the requirements for
the Degree of
MASTER OF SCIENCE
July, 2019

THE EFFECTS OF INJECTION ANGLE ON THE

STRUCTURE OF CHOKED GASEOUS JETS

Thesis Approved:

Dr. Khaled A. Sallam

Thesis Adviser

Dr. Arvind Santhanakrishnan

Dr. Krishnan Ranji Vaidyanathan

ACKNOWLEDGEMENTS

I would like to thank my wife for her support and patience throughout my pursuit of this graduate degree. Her love and encouragement have kept me motivated to complete this endeavor. I would like to thank my daughter for being my inspiration and helping to keep in perspective what really matters in life, family. I would like to thank Dr. Khaled Sallam for being an amazing mentor and friend. He was always patient and understanding of my obligations to both my family and of my fulltime employment throughout the entirety of my studies. I would like to thank Dr. Vaidyanathan and Dr. Santhanakrishnan for serving on my committee. I would like to thank my two lab mates: Saqib Raza and Andrew Williamson for their help in the initial set up of the apparatus, collection of the PIV images, and analyzing the experimental data. Last but not least, I would like to thank Dr. Mike Henneke and Dr. Shubham Srivastava for conducting a numerical simulation of the same nozzle geometry considered in this experimental study.

Name: ALEX MICHAEL SHERIDAN

Date of Degree: JULY, 2019

Title of Study: THE EFFECTS OF INJECTION ANGLE ON THE STRUCTURE OF CHOKED GASEOUS JETS

Major Field: MECHANICAL & AEROSPACE ENGINEERING

Abstract:

The effects of injection angle on the structure of choked gaseous jets injected into quiescent air is investigated experimentally. The study is motivated by the use of choked gaseous jets in many industrial applications, including gas turbines, flares, and burners. The test conditions were as follows: a choked gas jet injected into a quiescent air environment, a straight cylindrical nozzle with an exit diameter of 1.6 mm, and three (3) injection angles of 0° (normal injection), 15°, and 30°. The diagnostics included particle image velocimetry using pulsed Nd:YAG lasers. The jet was seeded with aluminum oxide (1-micron) particles and was injected into an environment that was seeded with water-based fog. The field of view was limited to 22mm × 22mm. The results included jet and entrainment flow velocities and vorticity fields. A computational study of the present three nozzles, by our collaborators, was used to validate and interpret the present experimental results. The experimental results showed that the increase of the injection angle of the nozzle, from the normal position, caused the jet structure to become asymmetric and partially blocked the nozzle exit. This was due to the generation of a velocity slip plane inside the injection port initiating at the leading edge of the inlet section of the nozzle. The sharp entrance edge of the nozzle acted as the nozzle's throat and triggered an expansion fan that accelerated the flow to supersonic speeds of Mach 1.4 for the present test conditions from a simple straight cylindrical nozzle without the use of the traditional convergent-divergent (De Laval) nozzle geometry.

TABLE OF CONTENTS

Chapter Page

LIST OF FIGURES

Figure Page

CHAPTER I

INTRODUCTION

1.1 Background

Effective mixing of various hydrocarbon compositions and oxygen is of interest for the purpose of achieving clean efficient combustion in the oil and gas industry. Combustion efficiency is of particular interest in industrial applications that introduce some level of combustion byproducts into the atmosphere such as furnaces and flare gas relief safety systems. The undesired byproducts produced by industrial applications of this nature are the result of imperfect combustion of the hydrocarbon gases being utilized. This is due to deficient stochiometric mixing of the hydrocarbon gas with oxygen resulting in incomplete combustion. Industrial processes of this type are regulated by the EPA and are mandated to comply with allowable emission rates [API 537, 2008]. Increasing the mixing efficiencies of industrial combustion equipment can further the effective destruction efficiency of the hydrocarbon gases used in these applications.

The use of choked jets is one method by which industrial combustion equipment increases mixing efficiency. Similar to a convergent-divergent nozzle which produces alternating expansion fans and shockwaves, a choked (sonic) gas jets triggers expansion fans at the exit of the nozzle followed by shock waves. Under-expanded convergent-divergent nozzles first trigger expansion fans while over-expanded nozzles will first trigger shockwaves. These shock waves play a critical role in jet mixing and control the characteristics of the flow field.

These localized mixing characteristics have been studied extensively for normal jet injection [Feranquet, 2015]. The theory of gas dynamics (Prandtl-Meyer / oblique shock waves) can be used to interpret the experimental data, including the size and location of Mach disks [John and Keith, 2006]. A concern, however, is the lack of information on inclined injection of choked jets. Due to space limitation in many industrial applications, designers often are forced to use inclined injection. Another concern is the effect of the port (injection nozzle) geometry on the jet mixing characteristics.

1.2 Problem Statement

In industrial applications it is not always advantageous or feasible to inject the fuel gas at an angle normal to the injection body. Further to these application restrictions it is of potential benefit for efficient mixing of hydrocarbon gas with surrounding oxygen to alter the angle of injection and/or the geometry of the nozzle with respect to the plan of the injection body. It is for these reasons that it is interesting to further understand the effect of the injection angle on the choked jet flow structure and jet mixing characteristics with ambient air. It is also of interest to further investigate the effects of the injector internal flow geometry on the maximum mass flux.

1.3 Specific Objective

The objectives of this study are:

1. To use laser diagnostics (PIV) to study the flow structure of inclined choked gas jets from cylindrical ports.
2. To understand the physics of the internal flow inside a choked port and its impact on the exit flow characteristics.

1.4 Organization of Thesis

The thesis includes 5 chapters as follows:

1. Chapter 1: Introduction - The background, problem statement, and specific objectives are presented.
2. Chapter 2: Literary Review - Past studies of choked jets are summarized in chapter 2.
3. Chapter 3: Experimental Methods - The experimental methods are detailed in chapter 3.
4. Chapter 4: Results and Discussions - The results are presented and discussed in chapter 4.
5. Chapter 5: Conclusions - Summary of results, conclusions and recommendations for future work are presented.

CHAPTER II

LITERARY REVIEW

2.1 Introduction

The study of under-expanded jets is extensive [Feranquet, 2015, Andre et al, 2014, and references cited within]. The applications include scramjet propulsion [Li, 2016 and 2017] and the efficient combustion of hydro-carbon gas releases for industrial applications [Chen 2018, Ruggles, 2012 and 2014]. The majority of these studies pertain to nozzles having some combination of converging-diverging geometry. Various non-conventional nozzle geometries have also been studied [e.g. Chen, 2018, Matsuo, 2018, and Otobe, 2008]. Various experimental methods currently exist for the collection of shock structure data and flow characteristic for small scale flows operating at sonic speeds. These techniques are explored in section 2.4. Unfortunately, there has been little work published pertaining to the use of these experimental method to study the structure of the near injector region of tilted and choked gas jets injected form cylindrical nozzles.

2.2 Symmetric Choked Jets

The shock structure of classic axisymmetric under-expanded jets is well known and can be explained through the use and implementation of the theories of gas dynamics [John and Keith, 2006]. Feranquet [2015] performed an exhaustive review of the major experimental studies pertaining to free under-expanded jets injected into a quiescent ambient environment noting that though much is well understood about the overall structure of under-expanded jets there are many

quantitative aspects which are not, including the Mach disk curvature, the location of entrainment initiation, the flow in the far field region, a fine resolution measurement of the turbulent vortices, and the turbulent transitions in the mixing layer.

The instability within the jet's flow structure assists in the promotion of mixing with the surrounding environment through the production of vortices [Andre, 2014]. Zapryagaev [2018] has proposed that a possible cause for streamwise vorticity creation at the shear layer of a supersonic under-expanded jet is due to Taylor- Görtler instability [Görtler, 1940] in the region and that the generation of these vortices are promoted by the nozzle surface roughness [Zapryagaev, 2018]. However, the Taylor-Görtler instability theory does not provide the needed resolution for accurate prediction of the turbulent kinetic energy or the flow structure produced by the developing vortices in the unstable mixing region. The mixing and entrainment properties of under-expanded jets are of practical interest. However, as noted by Feranquet [2015], mixing and entrainment properties are difficult to calculate. When considering multicomponent flow, e.g. Hydrogen injection in quiescent air, typical of scramjet engine applications, complex molecular diffusion affects the jet structure, mixing and vorticity characteristics [Buttay, 2018].

It is worth noting that slightly under-expanded jets behave similar to jets with highly subsonic Mach numbers [Andre, 2014]. Andre has observed that turbulence decreases as the Mach number increases due to the cell structure functioning as a turbulence suppressor [Andre, 2014].

2.3 Non-Conventional Choked Jets

Publications on non-conventional choked nozzle geometry (i.e. square, rectangular, elliptical, angled, etc.) are less prevalent than those on classic cylindrical nozzles. Chen [2018] conducted a thorough study on several non-conventional nozzle geometries including a simple straight jet injected at an angle of 45°. Observation of asymmetry in the flow structure was observed providing third party verification of the findings in the present study (Figure 2.3.1). Chen noted

that the observed asymmetric stagnation point of the investigated inclined jet aligned well with the results of Donalson and Snedeker's 1971 paper "A study of free jet Impingement" parts 1 and 2. It was determined that of all the nozzle geometries tested the 45° case (Y45) had the weakest nozzle pressure ratio (NPR) having dropped nearly 27% from that of the control case demonstrating that nozzle length is one of the most significant parameters in regards to pressure drop at a nozzle's exit. The Mach disk location was also observed to decrease and move closer to the nozzle's exit due the reduction in NPR and the presence of a second shock cell for the inclined 45° nozzle [Chen, 2018].

Chen [2018] also noted that the Y45 case had the largest deviation from that of the standard numerical models with respect to expected Mach disk diameter, deviating approximately 200%. Though, the Mach disk location of the Y45 nozzle did align well with the standard numerical models. It was also observed that the region adjacent to the angled nozzle exit acts as an impinging surface resulting in a reduction in Mach disk location and an increase to jet diameter [Chen, 2018]. It was observed that on the left side of the inclined jet's flow field the Görtler number was approximately 176 while the right-hand side of the jet was approximately 337 indicating asymmetric vortex patterns in the jet structure and providing clear indication of the existence of Taylor-Görtler instability. For elliptical nozzles it has been observed through the collection of pressure measurements at multiple locations downstream of the nozzle exit that the spread rate is greater in the minor-axis compared to that of the major-axis resulting in jet axes "switching" [Chauhan, 2015]. This jet axes "switching" was not observed in the present study confirming that the nozzles were of a hydraulically symmetric design.

2.4 Experimental Techniques

Being that the majority of the present research focuses on experimental data collection it is of particular importance to understand the currently available techniques used for the collection of small-scale (< 25mm x < 25mm) sonic flows. Several evaluation techniques exist for the

investigation of choked jet structures such as Raleigh Scattering [Panda, 1999 / Seaholtz, 2001 / Liu, 2018], Laser Doppler Velocimetry (LDV) [Kerhervé, 2004 / Meier, 2011], Laser Induced Fluorescence (LIF) [Zagidullin, 2015], background oriented Schlieren (BOS) [Iffa, 2011], and Particle-Image Velocimetry (as used in the present study) [Thielicke, 2014]. Each of the listed techniques are successful in deriving various flow characteristics. However, each of the techniques have their own strengths and weaknesses resulting in some being better suited than others in consideration for use in the present study.

Laser doppler velocimetry (LDV) and particle-image velocimetry (PIV) each utilize seeding particles entrained within the flow stream to determine flow characteristics. LDV is typically able to resolve data collection at a rate between 20 and 30 kHz [Meier, 2011]. LDV collection rates can be increased beyond this typical range but requires a larger density of seeding particles which can adversely affect the accuracy of the results [Seaholtz, 2001]. PIV experimental setups on the other hand are typically only able to resolve samples rates of between 3-10 kHz [Boxx, 2015 / Slabaugh, 2014] depending on the capability of the laser used and due to the needed time of the high-speed camera to upload its memory in preparation for collection of the next image pair. Slabaugh does note collection rates up to 20 kHz are possible when PIV is operated in burst-mode and is used in conjunction with a fiber oscillator, diode-pumped Nd:YAG amplifiers, and a secondary low-power high-repetition-rate laser as the master oscillator [Slabaugh, 2014]. As a note, at high flow accelerations these seeded flow techniques can be limited in their inability to resolve flows with high accuracy as the seeding particles can have difficulty tracking well with the flow field [Seaholtz, 2001].

LDV is typically used to compute mean velocity and turbulence intensity, but the measurements are not directly correlated to any time reference data making it difficult to evaluate the results with respect to time scales [Seaholtz, 2001]. Being that LDV takes measurements at a single point within the flow field where two beams cross the technique is well suited for small scale

flow. The only restriction being flows that are of a smaller width than that of the laser beams themselves. The technique is also well suited for sonic flows with Kerhervé able to resolve flows at Mach = 1.2 using LDV [Kerhervé, 2004].

PIV is typically used to compute the various velocity characteristics of an investigated flow (i.e. velocity in 'x' direction, velocity in 'y' direction, vortices location, turbulence intensity, etc.) [Andre, 2014]. Through the collection of large data sets of simultaneous flow measurements in a single 2D plane, PIV is able to produce highly accurate velocity profiles. The techniques implemented in PIV collection are also well suited for small scales sonic flows.

Rayleigh scattering is a nonintrusive alternate to that of the seeded LDV and PIV approaches as it requires no flow seeding. Instead of using seeding particles the Rayleigh scattering technique relies on light spectrum diffraction due to interaction between a laser beam and the molecules of the gas flow field [Panda, 1999]. Rayleigh scattering can determine velocity, density, and temperature gradients of an investigated flow. Temperature is derived through correlation with the width of the Rayleigh spectrum, density is proportional to total scattered light, and the velocity components are proportional to the shift of spectral peak from the frequency of the incident light. As a note, Rayleigh scattering is reliant on knowing the gas composition as the spectral width is a function of molecular weight of the gas [Seaholtz, 2001]. Through the use of Rayleigh scattering techniques Liu [2018] was able to resolves flows at Mach 3 (Figure 2.4.1) at a collection rate of 10 kHz in a viewing window of 12.5mm [Liu, 2018].

Laser induced fluorescence (LIF) is an additional technique used for the investigation of flow characteristics. LIF can derive density, composition, and mixing but is unable to evaluate velocity (Figure 2.4.2). The quality of LIF collected data is heavily reliant on both high density of gas within the window of investigation and a good understanding of the flow particle's fluorescent decay rate [Zagidullin, 2015]. Schlieren imaging is also a valuable technique to utilize in the

evaluation of flow structures. Schlieren is able to provide density data through visualization of the flow structure (Figure 2.3.1 and 2.4.3). Through this visualization of density an observer can accurately measure shock structure and shock angles within the flow [Venkatakrishnan, 2005].

In the present study PIV was selected for flow diagnostics as it was well suited for the present test conditions and was readily available in the OSU-Tulsa laboratory where the experiments where performed. A PIV experimental setup was also attractive for its relatively low cost of the needed equipment and image processing software. It will be shown in the present study that velocities of Mach = 1.4 and viewing windows of $\leq$ 25mm $\times$ 25mm can be derived with high resolution using PIV.

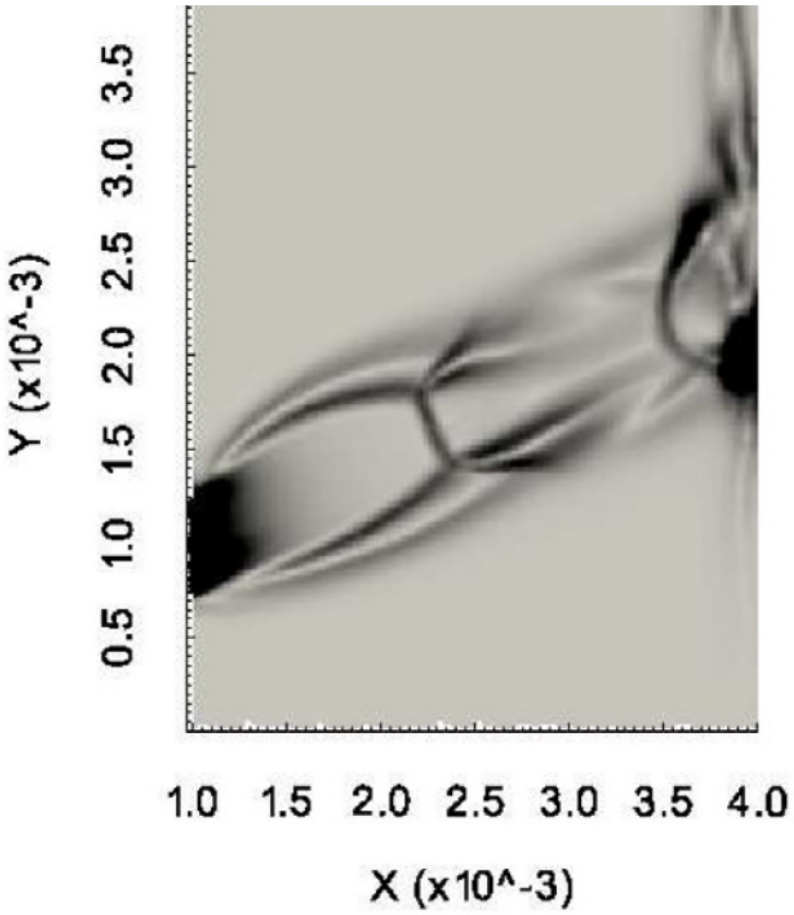

Figure 2.3.1 – Schlieren Density gradient for the 45° (Y45) nozzle depicting jet expansion. Density color scaling from 100 to $8x10^4$. (Source: Chen, 2018 - Figure 5.d)

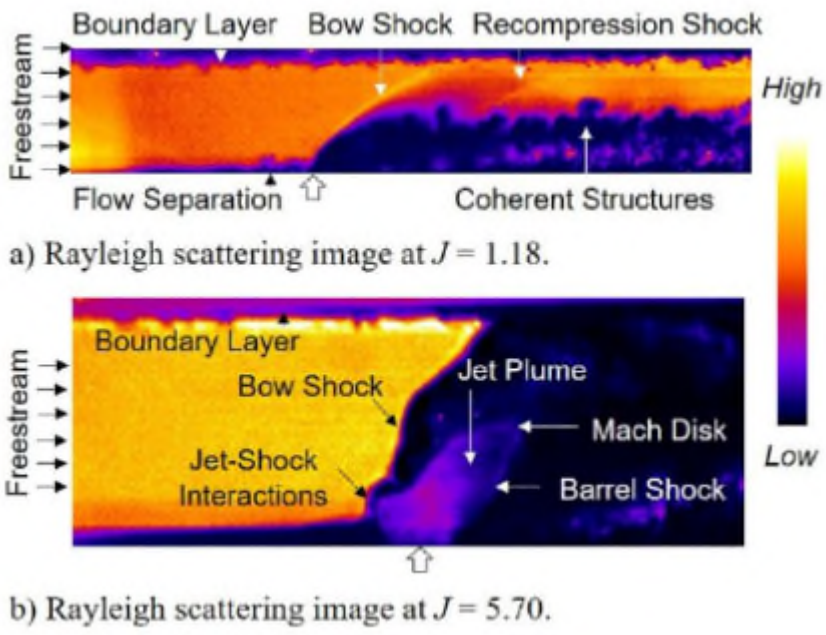

Figure 2.4.1 – Rayleigh scattering image of flow at Mach = 3 where J is the jet-to-freestream momentum ratio (Source: Liu, 2018 - Figure 3)

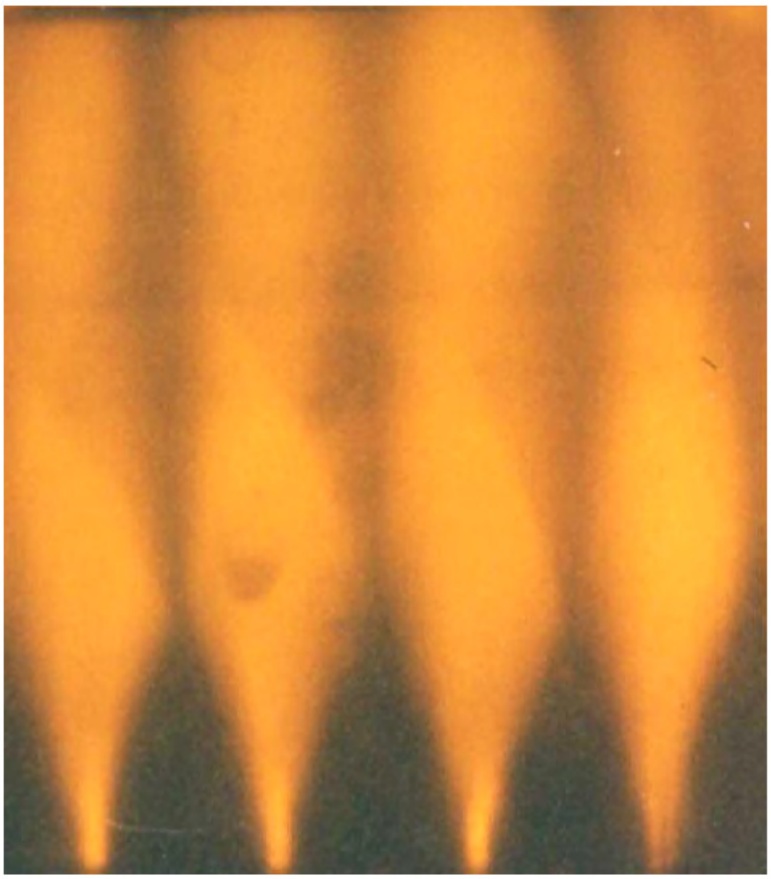

Figure 2.4.2 – Laser Induced Fluorescence flow density (Source: Zagidullia, 2015 - Figure 1)

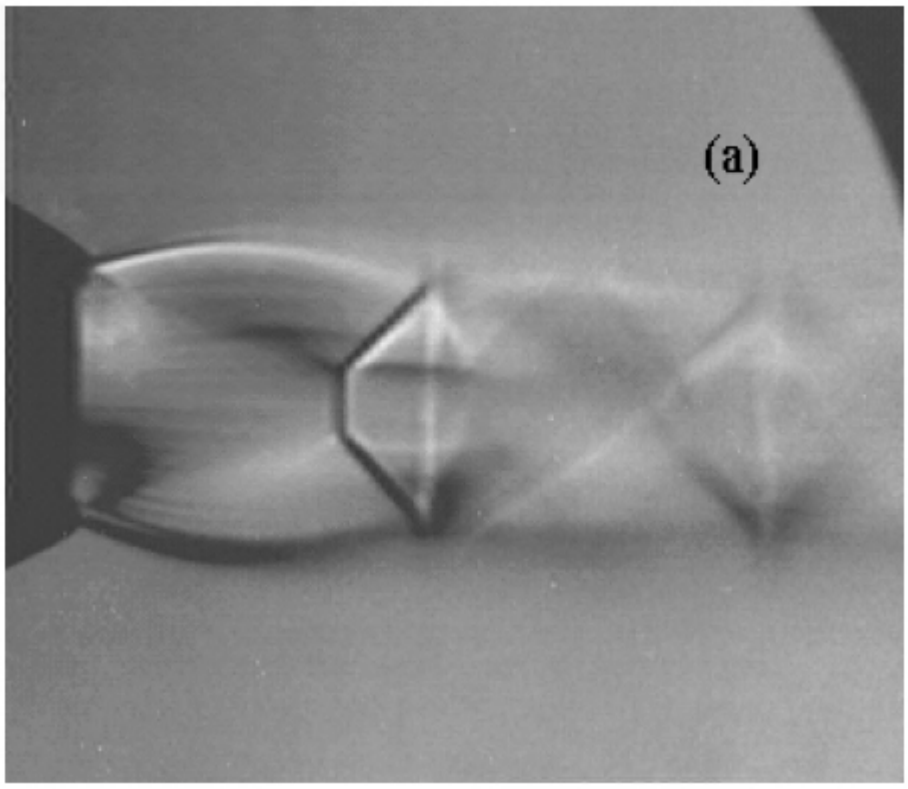

Figure 2.4.3 – Conventional Schlieren image of 36mm under-expanded jet at M = 2.5 and NPR = 6 (Source: Venkatakrishnan, 2005 - Figure 10.a)

CHAPTER III

EXPERIMENTAL METHODS

3.1 Introduction

This chapter covers the experimental methods used to evaluate the mixing characteristics of under-expanded choked jets injected into atmospheric pressure. Topics covered include the test apparatus designed and used for the experiment, the system calibration required to obtain high quality PIV images, and PIV computational method [Thielicke, 2014].

3.2 Apparatus

This section describes the apparatus used to test the nozzles (Figure 3.2.1). The experimental setup used for this research is multifaceted containing several systems that are separate but used in conjunction with each other to collect data. The various systems include a pressure delivery and seeding system, laser and laser sheet optics, and a triggered PIV camera used to capture the image pairs. See Fig 3.2.2 and 3.2.3 for a diagram representation and image of the overall PIV system.

3.2a Pressure Delivery and Seeding

The pressure delivery system for the experimental setup consists of many key components. First of which is the solid particle seeding chamber. The nozzle to be tested is mounted in the top of the seeding chamber via a 1” NPT threaded connection (Figure 3.2.1, 3.2a.1, and 3.2a.2). A pressure gauge (PG-201) (Figure 3.2a.3) is mounted just upstream of the orifice to measure

chamber pressure (p_0). This pressure is critical as it is the variable used to determine if the chamber pressure is high enough to achieve choked flow through the nozzle as it relieves to the ambient condition. The minimum required operating pressure to confirm choked flow is further discussed in Section 4.2a. The chamber pressure is also used to confirm that the relief pressure through the test orifice is constant throughout the testing period resulting in consistent velocity magnitudes.

Aluminum oxide seeding particles (ALOX #1MIC – Linde C from Beta Diamond Products, Inc.) were kept at the base of the chamber. These particles have a nominal diameter of approximately 1 μm (Fig. 3.2a.4). Due to the particle's size and density they are easily entrained by the flow within the chamber prior to exiting through the test nozzle. The particles have little inertia and therefor closely mimic the flow properties of the air at and downstream of the injection site. The solid particle seeding chamber sits on top of a Variomag brand seeding agitator (SG-101). The seeding agitator spins an oblong shaped magnet inside the seeding particle reservoir. The spinning magnet helps to continually churn up the seeding particles resulting in reduced powder clumping and a more consistent seeding density exiting the test nozzle.

It was noticed during the initial testing phase of the project that the aluminum oxide particles did not disperse into the environment surrounding the jet profile well enough for the PIV software to accurately account for environmental entrainment and mixing by the jet; as seen in Fig. 3.2a.5. This was mitigated by the introduction of atomized water vapor, as seen in Fig. 3.2a.6, to track the interaction of the choked jet with the ambient air. A fog machine was used (AMERICAN-DJ 400w Fogger) to saturate the environment with water vapor. The presence of the water vapor greatly increased the ability of the PIV software to capture the interaction of the choked jet with the ambient air. As the choked flow exits the nozzle the outer profile of the jet interacts with the water vapor. The resultant expansion fans caused the water vapor droplets to move away from the nozzle while the returning oblique shock waves pull the water droplets back in toward the center of the jet.

The volumetric flowrate exiting the nozzle [L/h] was measured upstream of the seeder by a set of parallel rotameters (Omega Tube Model: FL-1448-S and 044-40-N) (Figure 3.2a.7). The sight glass on the rotameter has a scaled marking system that directly relates to a manufacturer correlation chart, as shown in appendix Figure A.1.1 and A.1.2, which is used to determine the volumetric flow rate through the meter for various fluids and gases. The reading from the rotameter is an important variable to confirm the expected theoretical flow rate exiting the nozzle is achieved as discussed further in Section 4.2b. When the flow rate as indicated by the rotameter closely matches the theoretically expected flow rate it helps to further increase confidence that there are no leaks in the air delivery system of the seeder. The measured volumetric flow rate from the rotameter can be used with the pressure reading from pressure gauge (PG-201) and the known ambient temperature to calculate the mass flow rate through the orifice. The mass flow rate is of value in determining the consumption rate of utility air by the orifice. In the petrochemical and oil industry mass consumption is critical for the use of calculating overall utility costs.

Upstream of the rotameter is a 20-gallon utility air accumulation tank. This tank is used as a buffer for pressure throttling purposes when setting the chamber pressure (p_0) and the orifice exit pressure (p^*). The accumulation tank is an ASME stamped Section VIII compliant pressure vessel rated up to 800psig of continual containment. The accumulation tank is protected by a pressure safety valve (PSV-101) set at 200psig to comply with ASME Section VIII emergency fire case relieving requirements. A pressure gauge was mounted between the air accumulation tank and the rotameter to measure accumulated pressure in the tank. Without the accumulated volume of compressed air in the accumulation tank the pressure in the chamber would fluctuate rapidly due to minor variations in feed pressure. These fluctuations can occur from supply feed pressure droop or from the operator opening or closing the control needle valve (NV-101) or the pressure control valve (PCV-101) (Figure 3.2a.8) to adjust the pressure in the chamber.

The primary supply pressure of utility air to the lab in which the experiments were conducted was 110 psig. This pressure was reduced by a pressure control valve (PCV-101) to achieve a constant pressure inside the chamber during testing. This constant chamber pressure insured that the exit velocity of the seeding particles through the test orifice were consistent throughout the testing period. This is a critical variable to maintain. If the particle velocity changes throughout the testing period, the PIV software discussed in Section 3.5 is unable to properly determine the mean velocity vector magnitudes accurately.

The critical considerations for this portion of the experimental set up are twofold. The first of which is maintaining constant chamber pressure (p_0). The chamber pressure must at a minimum be above the minimum exit pressure (p^*) divided by 0.5283 (for air) to achieve choked flow through the orifice. The second consideration is to maintain consistent particle seeding density in both the orifice exit stream and the atmospheric environment into which the nozzle is ejecting. Uniform particle seeding density in both the stream and the environment helps produce high quality results by the PIV software discussed in Section 3.5

3.2b Laser and Optics

Class IV lasers (Nd:YAG, New Wave model: SOLO III PIV) (Figure 3.2b.1 and 3.2.3) and several optical elements are used to generate a laser sheet to illuminate the seeding particles / fog discussed in Section 3.2a. These two laser pulses, when triggered in conjunction with two highspeed camera frames, are used to produce the necessary particle illumination for the capturing of the PIV image pairs (Figure 3.2b.2). Nd:YAG lasers are well suited for PIV setups specifically for their ability to produce high-powered beams with short pulse durations. The laser used in this experiment can produce beams of up to 70mJ/pulse in strength. The Nd:YAG (neodymium-doped yttrium aluminum garnet; Nd:$Y_3Al_5O_{12}$) crystal is the lasing medium used to produce the laser pulses [Koechner, 2006]. The Nd:YAG laser was operated in Q-switching mode for this experiment. In this mode the laser uses an optical switch located in the laser cavity. This switch

does not open until the maximum population inversion of ions has been achieved [Koechner, 2006]. The light wave, which has a wavelength of ~1064 nm, passes through the Q-switch cavity de-populating ions in the excited neodymium medium at maximum population inversion [Koechner, 2006]. The short pulse duration, as short as 5 ns, allows for crisp "frozen" images of the fast-moving particles which reduces streaking of particles in the images even when they are moving at supersonic speeds.

Two separate laser pulses with a preset pulse separation (ΔT) are triggered across the flow field perpendicular to the camera lens. The two lasers used in the present setup are armed and triggered from an external programmable triggering device discussed in detail in Section 3.2c. A photodiode (PD-101) was used in conjunction with an oscilloscope (Lecroy Model: 9314L Quad 300 MHz) to confirm that the actual laser pulse separation was correct and that the camera trigger was appropriately aligned (Figure 3.2b.3). Having a short period between pulses (pulse separation) allows for the capture of PIV image pairs for flows at supersonic velocities and small observation widows. The limitation on pulse separation is usually imposed by the capability of the camera and the delay generator.

In this experiment the observation window of the PIV captured images is 22mm x 22mm and the pulse separation was set at 0.5μs (2,000,000 frames/sec for double-exposure) to capture the main jet. Flow velocities with M = 1.3 were observed at the set laser pulse separation of 0.5 μs. A pulse separation of 10 μs was used to capture the entrainment flow which allowed for visual and computational confirmation that the environment that the test nozzle was ejecting into was not affected by outside factors beyond the primary jet nozzle. At particle velocities of M = 1.3 and a ΔT between pulses / images of 0.5μs the particles are displaced from image A to image B in a captured PIV image pair by ~0.19 mm or ~1% of the overall observation widow. An ~1% field displacement of particles between images of a PIV image set is preferred [Thielicke, 2014] as the

PIV processing software, discussed in Section 3.5, can more accurately track particles between image A and B and produce high resolution results.

Three optical elements where used in the experimental setup. Upon leaving the laser body the beam passes through a mirror that redirects the beam 90° in the clockwise direction (Figure 3.2b.4). This mirror was needed to change the direction of the beam to be perpendicular to the camera lens. The laser body discharge direction was placed in the same plane as the camera due to limited laser and optic mounting space. Second the redirected beam passes through a cylindrical lens used to convert the beam into a sheet. Finally, the sheet passes through a spherical lens (Figure 3.2b.5) used to focus the sheet such that it was as thin and intense as possible as it passes through the nozzle flow field (the nozzle is only 1/16" dia.) and in front of the observation window of the camera (Figure 3.2b.6 thru 3.2b.8). By making the laser sheet as thin as possible the potential for illuminating particles outside of the point within the orifice flow field that the camera is focused on is reduced. Out of focus particles captured in PIV image sets adversely affect the accuracy of the PIV processing software. It is also important that the focal point of the laser sheet be set at the camera's observational window so that the intensity of the laser is highest within the observation window resulting in well illuminated seeding particles. As the laser sheets hits the seeding particles they illuminate resulting in light spots that appear to be 40 to 50μm in diameter in the captured images. This increase in observable diameter from the actual 1μm particle diameter allows the seeding particles (in a large field of view relative to particle diameter) to be easily captured by a camera with a limited array size (typ. 2048 x 2048 pixels) and be successfully evaluated by the PIV processing software. Calibration of lens placement is discussed further in Section 3.3.

3.2c Camera and Pulse Generator

A double-exposure CCD camera (PCO Power Model: PCO.2000, Cooled 14bit, 2048 x 2048 pixels) with a Nikon AF Micro Nikkor 60mm (1:2.8 D) lens (Figures 3.2c.1 and 3.2c.2) was positioned perpendicular to the laser sheet. This CCD camera captures paired image sets. Each

image within a pair is synchronized with a dedicated laser pulse; Image A and Image B. In this experiment the time separation between Image A and Image B was set to 0.5μs. The known ΔT (0.5μs) between the two images allows the PIV processing software to calculate particle velocity after measuring particle displacement between Image A and Image B of a given PIV image pair.

More accurate velocity and mixing characteristic of the flow can be calculated as more image pairs of a given test condition are evaluated by the PIV processing software. The effect of the number of collected image pairs on the results can be seen in Figures 3.2c.3 thru 3.2c.5. Figure 3.2c.3 shows the average velocity component in the 'u' direction for 125 image pairs, Figure 3.2c.4 shows the same evaluation for 250 pairs, and finally Figure 3.2c.5 shows the highest averaged magnitude resolution taking into considering 500 image pairs. As can be seen when comparing the three figures the resolution increases as more pairs are added to the evaluated data set.

Synchronization of the two camera exposures with the two laser pulses was controlled by a programmable eight channel pulse generator (Make: Quantum Composers / Model: 9518). The delay generator allows the user to define the trigger time of each device based on a time delay starting from T = 0. Figure 3.2c.6 depicts the triggered time delay of each device. The first device triggered is the CCD camera. The camera is triggered at T = 300μs for a period of 195μs. This allows time for the aperture of the camera to open prior to production of the first laser pulse. In Q-switch mode the Nd:YAG crystal's Q-switch is first triggered and then at a specified time the Q-switch is demanded open and the laser fires.

As seen in Figure 3.2c.6 the trigger for laser A is activated by the delay generator at 127.5μs (T = 372.75μs) before the camera trigger completes. The Q-switch for laser A is then triggered 127μs later (T = 499.75μs) just 0.5μs before the camera trigger completes. Laser B is activated 112μs (T = 387.25μs) before the camera trigger completes and the Q-switch is fired at the same moment the camera trigger finishes (T = 500.25μs) resulting in a ΔT between Image A and Image

B of 0.5μs. The second camera exposure occurs after the camera trigger completes and thus the second laser pulse happens 0.25μs after the camera trigger completes. The aperture of the camera stays open during the second exposure until the camera memory download is completed.

3.3 System Calibration

The production of quality PIV image pairs is reliant on proper calibration of the various independent systems of the test setup (i.e. pressure delivery system, camera, laser, optics, and pulse generator). If each of the component of the system is not properly calibrated the resultant PIV image pairs will be of a sub-optimal quality and cause incorrect and / or skewed results by the PIVLab processing software utilized in this study as discussed in Section 3.4.

3.3a Calibration of the Pressure Delivery System

Achieving relative steady state pressure delivery to the orifice throughout an image collection session is critical for validation of constant nozzle exit pressure (p^*) and particle velocity. If the delivered pressure changes during an image collection session the average particle velocity and exit pressure from the nozzle changes accordingly resulting in skewed results by the PIV processing software. Pressure fluctuations during a test cycle can also adversely affect the consistency of seeding particle density exiting the test nozzle.

To reduce fluctuations in air pressure delivered to the test orifice an air accumulation tank, a pressure control valve, and a throttling needle valve are placed upstream of the particle seeding chamber. A 20-gallon air accumulation tank is used to provide a relatively large volume of compressed air for delivery to the test orifice. The accumulated compressed volume of air in the tank reduces rapid pressure fluctuation to the orifice due to periodic pressure delivery droop from the main 110psig supply and / or the pressure control valve (PCV-101). The pressure control valve (PCV-101) is used to reduce the primary feed pressure of air in the lab from 110psig to a pressure that allows for steady state delivery of pressure to the orifice to achieve choked flow.

As discussed in Section 4.2 (Eq. 4.2a.3) a minimum p^* of ~28 psia is required to achieve choked flow through a 1/16" dia. orifice discharging into a downstream environment at atmospheric pressure. A throttling needle valve (NV-401) is used to achieve a min. pressure delivery to the orifice of 28 psia as indicated by the pressure gauge (PG-201) just upstream of the orifice outlet. Once the minimum pressure is confirmed by the throttling of NV-401, PCV-101 is set to a delivery pressure to the accumulation tank that allows for a steady state pressure indication at PG-201 over a calibration period of 10 minutes. After PG-201 indicates a constant pressure at the nozzle chamber throughout the calibration period it is confirmed that the pressure delivery system has achieved equilibrium and has been properly calibrated.

It is also important to confirm that the instrument air delivery system has no leaks. This is accomplished by comparing the volumetric flow rate as indicated by the rotameter and the calculated theoretical volumetric flow rate as discussed in Section 4.2 (Eq. 4.2b.1). Per equation 4.2b.1 it is calculated that for an exit pressure of ~27 psia through a 1/16" dia. orifice into a downstream environment at atmospheric pressure the corresponding theoretical volumetric flow rate will be 66.4 SCFH. During the experiment the rotameter indicated a measured volumetric flow rate of approximately 31.6 L/m at standard conditions (66.8 SCFH) delivered to the orifice indicating negligible leaks in the delivery system.

3.3b Calibration of Camera, Laser, and Optics

In addition to proper calibration of the pressure deliver system; accurate tuning of the image collection components is highly critical. As with the pressure delivery system it is important that the focal plan of the camera lens, the position of the laser sheet w.r.t to the camera and orifice exit, and the position of the orifice exit within the collected image pairs are all constant throughout the imaging session. This consistency insures quality results from the PIV processing software.

The first step in proper calibration of the imaging components of the PIV system is to set the focal plan of the camera lens to its ideal focal distance, or where the lens produces the sharpest images. This ideal focal distance (u_n; the distance measured between the camera lens and orifice) can be calculated using the following equation [Douvos, 2013]:

$$N_{ideal} = \sqrt{375 * \left(\frac{u_n f}{u_n - f} - \frac{u_f f}{u_f - f}\right)} \tag{3.3a}$$

where $N_{ideal} = ideal\ focal\ number$, $u_f = distance\ to\ image\ of\ far\ object$, and $f = focal\ length\ (fl)$. For this application a Nikkor AF Micro 60mm 1:2.8D model lens was used and with manual focusing selected. Noting that the test orifice has a diameter of 1/16" (~1.6 mm) and the laser sheet is focused to approximately the same thickness; the delta between u_n and u_f is known to be 1/16". The lens used has a focal length (f) of 60mm and a pre-set focal number range (f-stop) from f/2.8 to f/32.

Using equation 3.3a in consideration with the above we find that the ideal distance $u_n = 150mm$ as measured from the camera lens at an f-stop setting of f/16. The denominator of the f-stop setting represents the diameter of the aperture. For the 60mm lens used the corresponding aperture diameter at an f-stop setting of f/16 is 3.75mm (60mm/16). The f-stop setting of f/16 was selected to both reduce over exposure of the images which can result in a "bleeding" effect of the captured illuminated seeding particles and to keep the depth of field as narrow as possible to reduce the number of transient particles being captured from one image to the next as they enter and exit the field of focus / laser sheet. The lower the f-stop number (i.e. f/10 = 6) the narrower the depth of field and darker the image. The higher the f-stop number (i.e. f/2 = 30) the wider the depth of field and brighter the image.

Once the orifice was placed at the calculated ideal distance from the camera lens (u_n); the height of the orifice in the field of view was selected and set to achieve the desired range in the

vertical (v) direction of the flow filed for PIV evaluation. A USAF / RoHS compliant resolution target (Edmund Optics Model #: 38-710) (Figure3.3b.1) was then placed at the centerline of the orifice, perpendicular to the camera lens, and in line with the direction of the laser sheet. The smallest element that could be focused on was Group 3 Element 4 defining a resolution of 39μm. The focal plan used in the present setup resulted in images of 22 mm x 22 mm in size.

Once the orifice is set to the optimal distance from the camera lens to achieve the sharpest possible images the laser and corresponding optics can be positioned. There are several critical parameters to consider when tuning the laser optics to achieve high quality and consistent images. As previously referenced several optical lenses are used in conjunction with the Nd:YAG laser for redirection and shaping. It is important that these lenses be regularly cleaned to avoid damage to them and unwanted diffraction of the laser beam.

The laser beam first passes through a cylindrical lens used to convert the beam into a sheet. The orientation of the cylindrical lens is perpendicular to that of the orifice ejection angle. This allows for the production of a laser sheet that is in the same plane as the orifice and perpendicular to the camera lens. The laser sheet then passes through a spherical lens used to focus and set the thickness of the sheet. The laser sheet is set to a thickness as close as possible to the depth to which the camera lens is focused to avoid illuminating transient particles outside of the primary flow field. In this case the diameter of the orifice (1/16”) outlet is used. This sheet thickness setting is accomplished through altering the distance between the cylindrical and spherical lenses. In addition to sheet thickness it is also important that the distance between the orifice and the spherical lens is set to the focal distance of the spherical lens. This insures the most intense portion of the laser sheet is passing through the camera’s field of view resulting in the highest particle illumination possible.

3.4 PIV Image Processing

The captured image pairs where processed using a free MATLAB based software toolbox titled “PIVLab” [Thielicke, 2019]. A large number of image pairs (500 – 1000) where captured for each of the three nozzles tested in this study (*0°, 15°, and 30°*). These large image pair sets where used to increase confidence that the software was calculating accurate flow characteristics. The software indicates measured velocity vectors in green while missing vectors interpolated by PIVLab are shown in orange [Figure 4.3.3]. There were very few interpolated vectors which indicates satisfactory jet seeding and particle entrainment.

PIVLab was used to also calculate entrainment flow from the atmosphere into the primary jet column, the velocity magnitude of the jet, the horizontal (u) and vertical (v) velocity components, the vorticity magnitude, and the location of jet vortices to indicate the location of the expected Mach diamonds. Postprocessing of the results required placing realistic filtering limitation on the velocity vectors as well as using a smoothing filter to account for missing vectors.

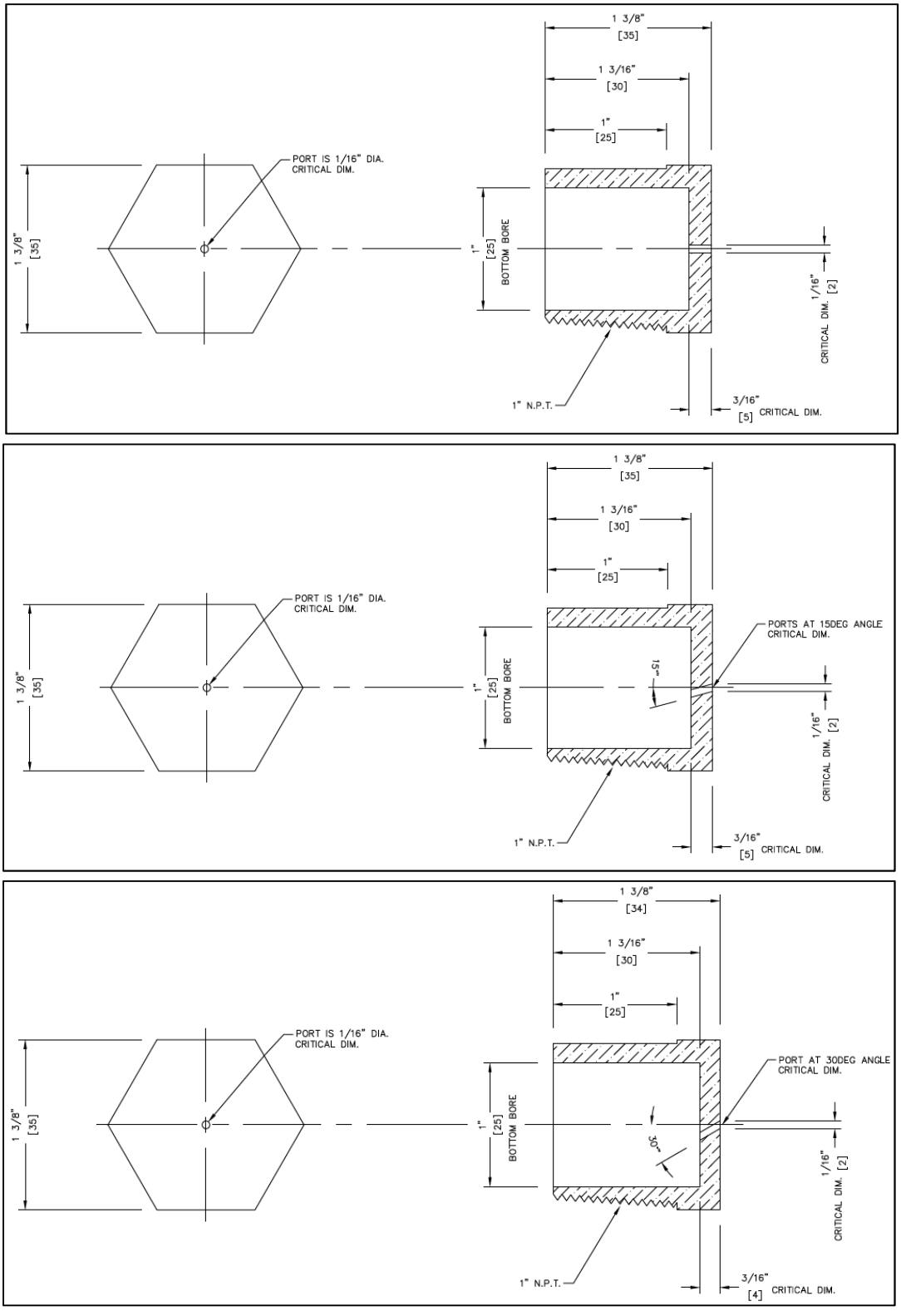

Figure 3.2.1 – Diagram of Test Nozzles (Top: 0°, Middle: 15°, Bottom: 30°).

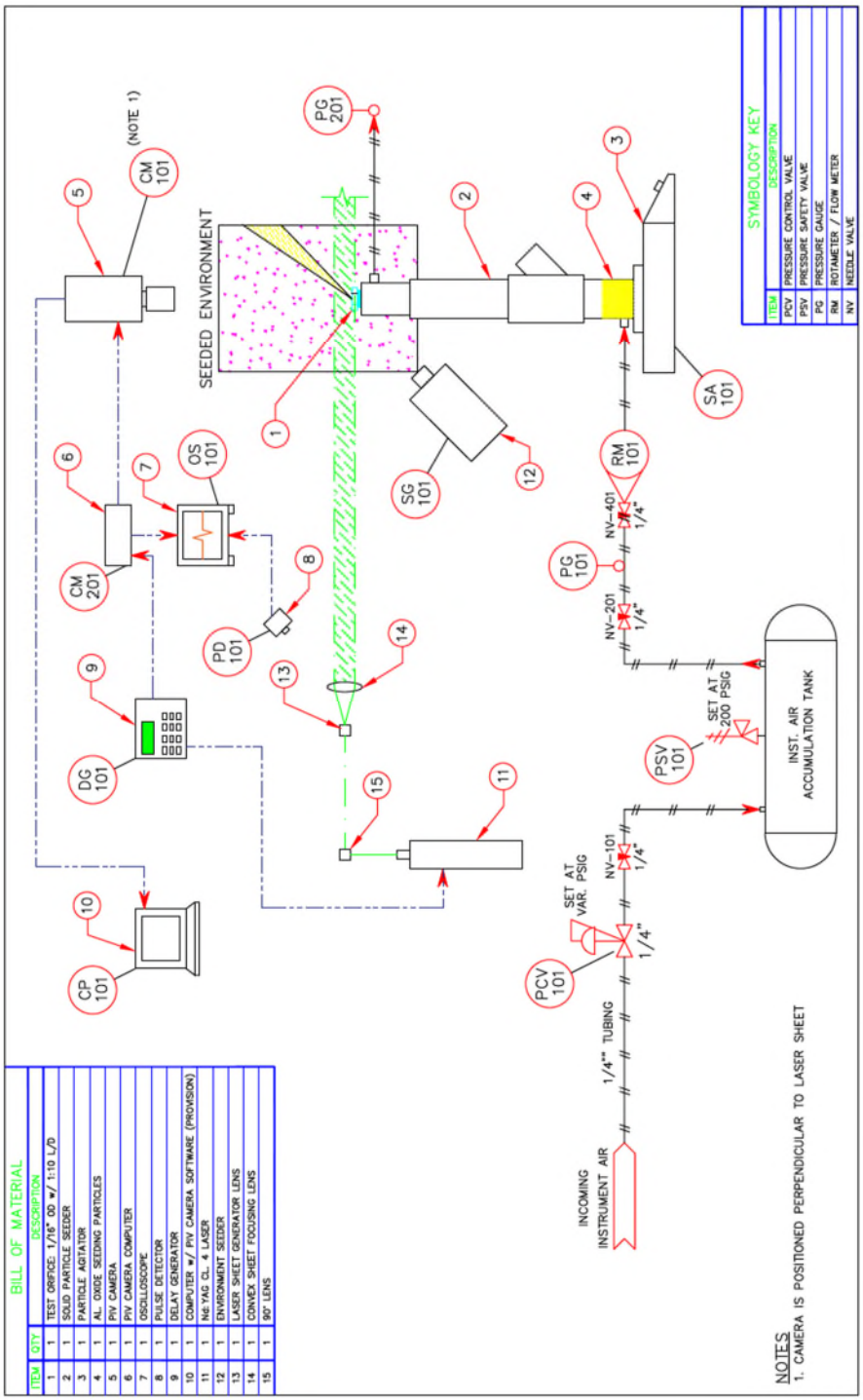

Figure 3.2.2 – Diagram of Experimental Setup.

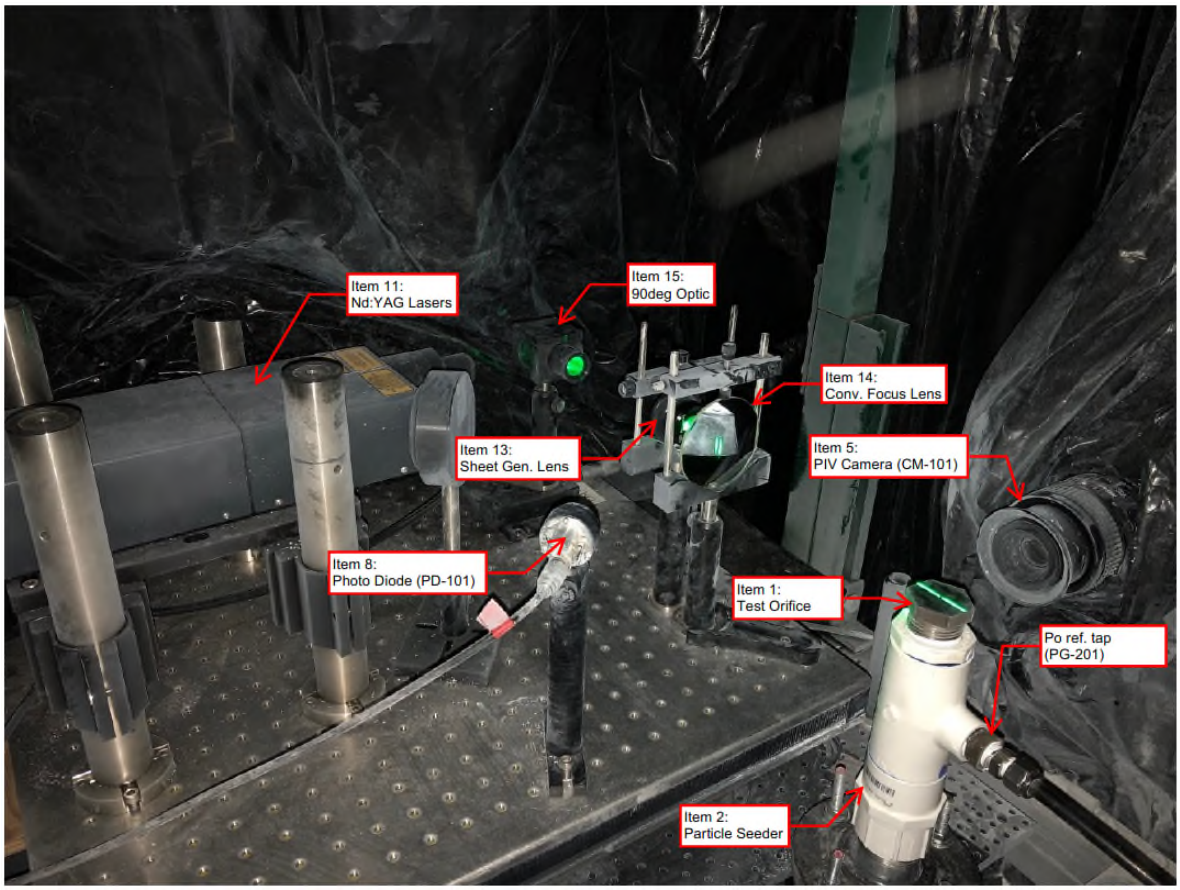

Figure 3.2.3 – Image of Experimental Setup (pressure delivery system not shown).

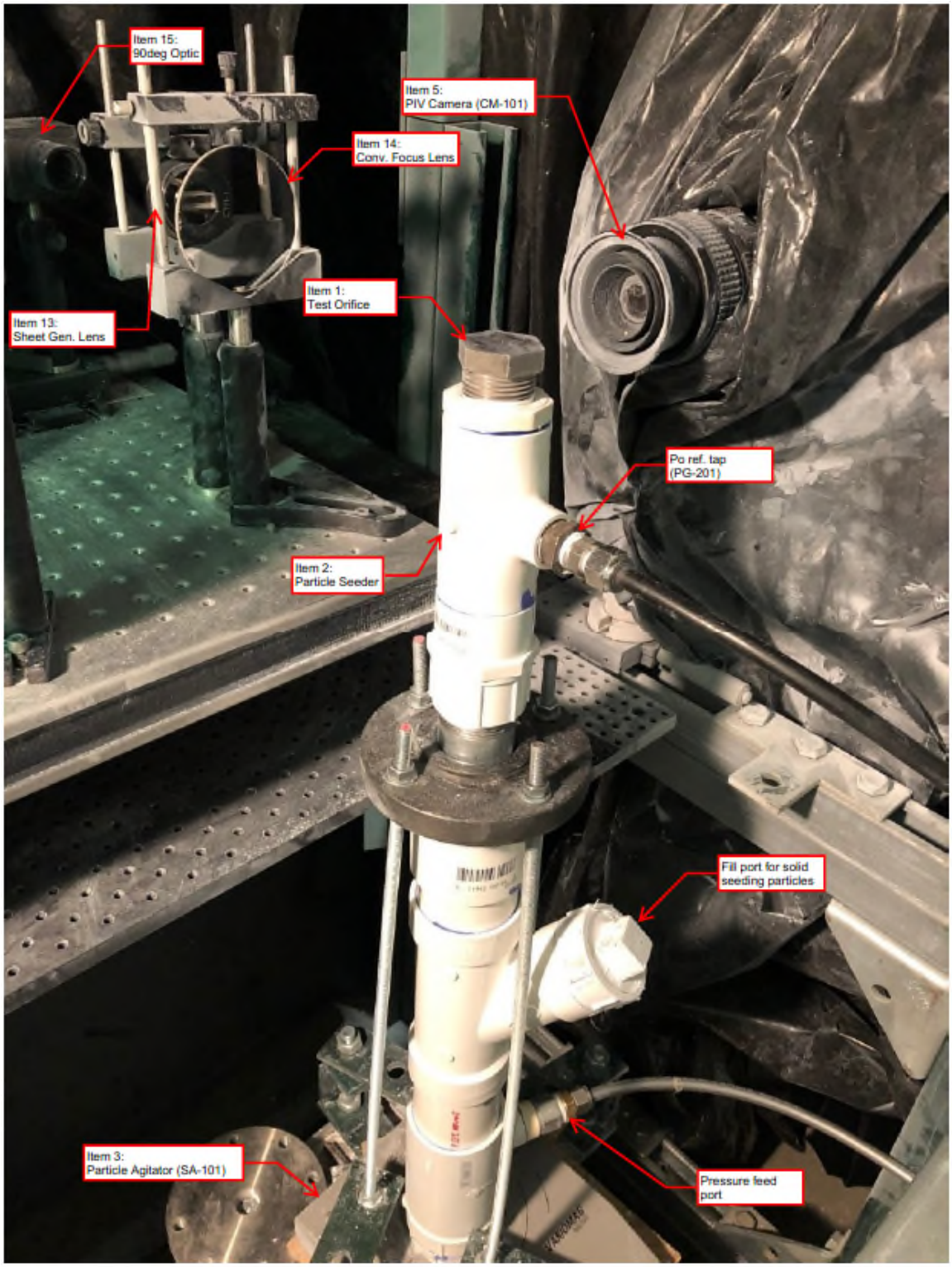

Figure 3.2a.1 – Particle Seeder with test orifice installed, PIV camera and laser optics in background, sitting on top of the seeding agitator (SG-101), feed pressure entering at base (silver hose), and (PI-201) pressure reference line (black hose) just upstream of nozzle exit.

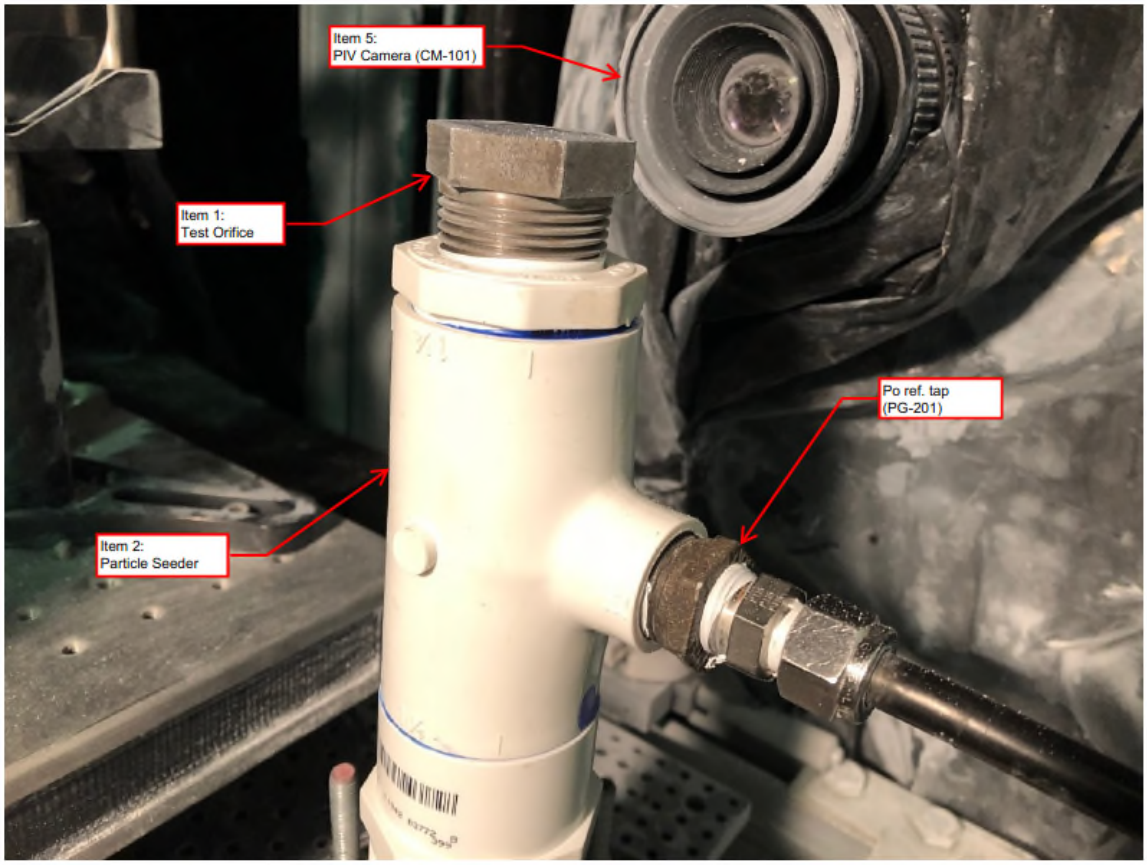

Figure 3.2a.2 – Close up of test orifice installed in particle seeder with PIV camera in background and PI-201 pressure reference line entering from the right of the image.

Figure 3.2a.3 – PG-201 pressure gauge measuring the pressure up steam of the nozzle exit.

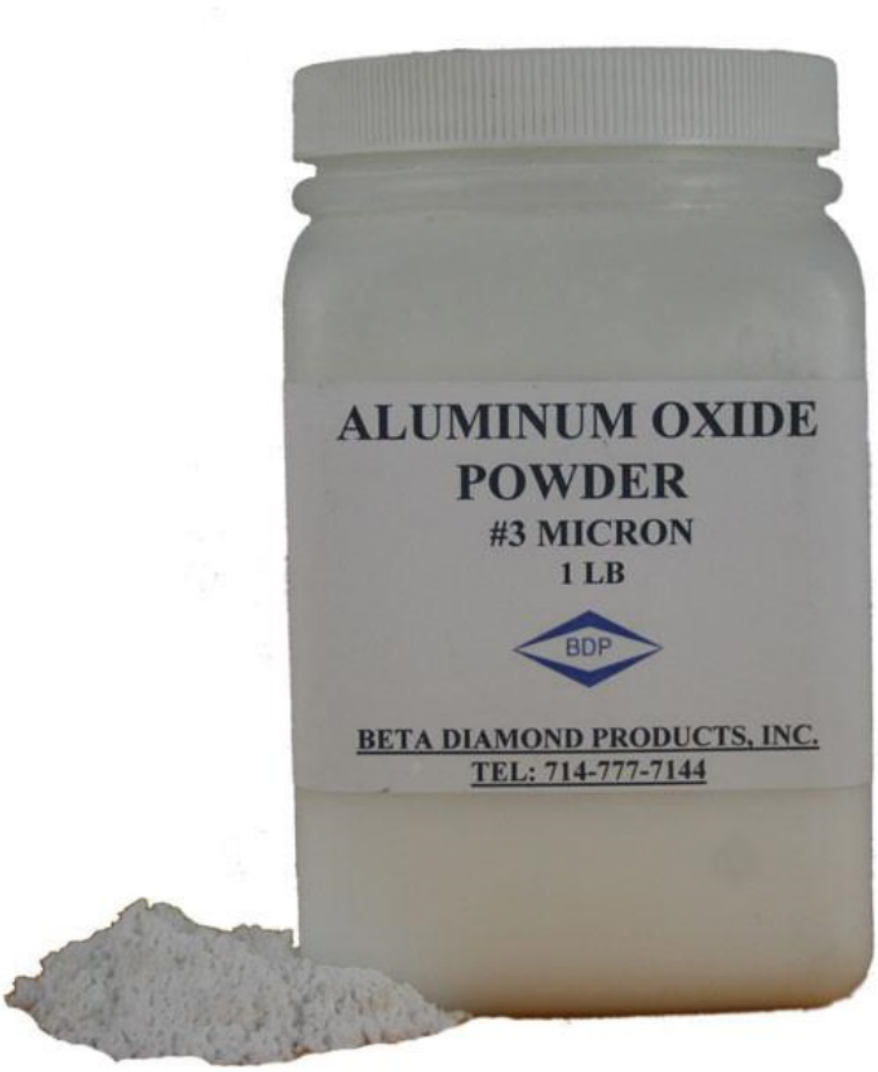

3.2a.4 - ALOX #1MIC – Linde C from Beta Diamond Products, Inc.

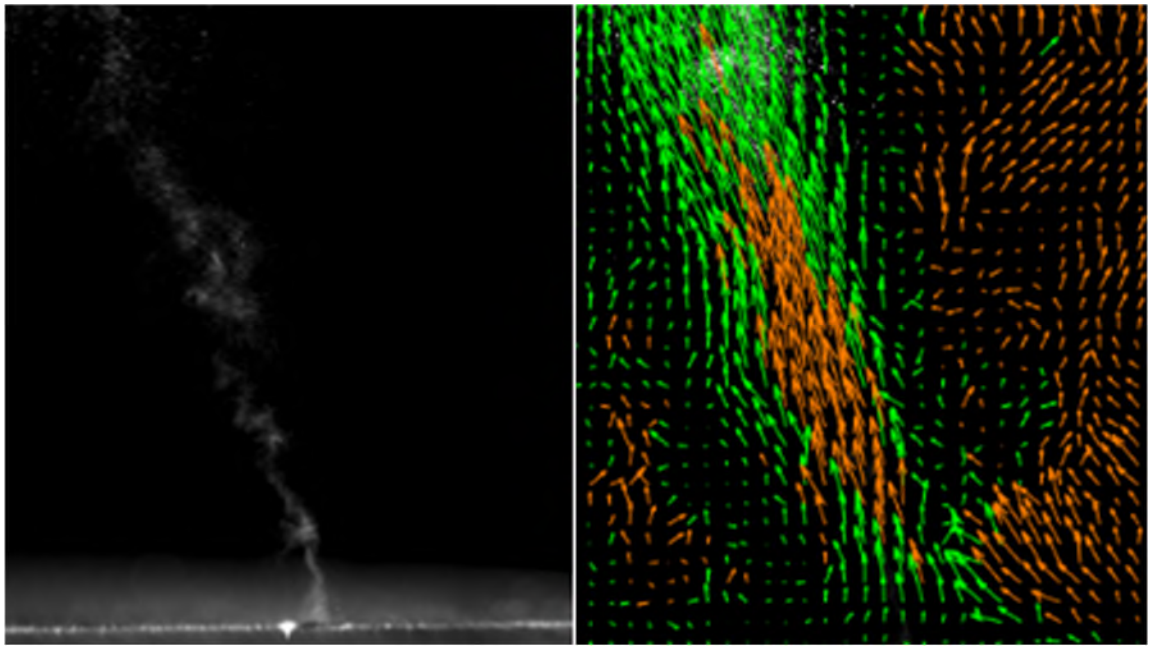

3.2a.5 – Left: Image of the flow field with internal seeding only without external fog seeding. Right: Wrong interpolated velocity vectors due to the lack of the external seeding.

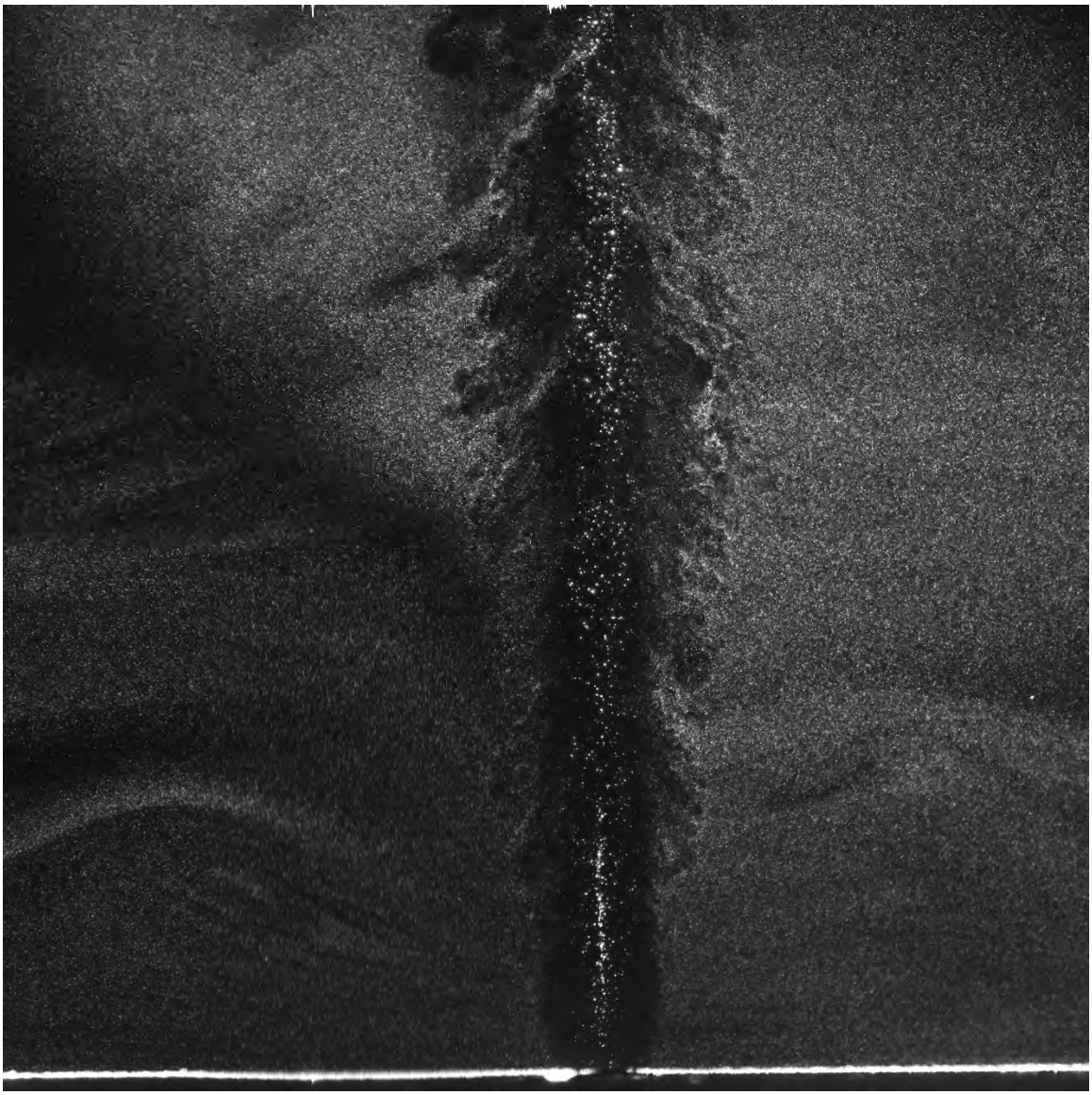

Figure 3.2a.6 - Example of image collected for a vertical (°0) single choked jet nozzle discharging 1[μm] aluminum oxide particles into a water vapor saturated environment.

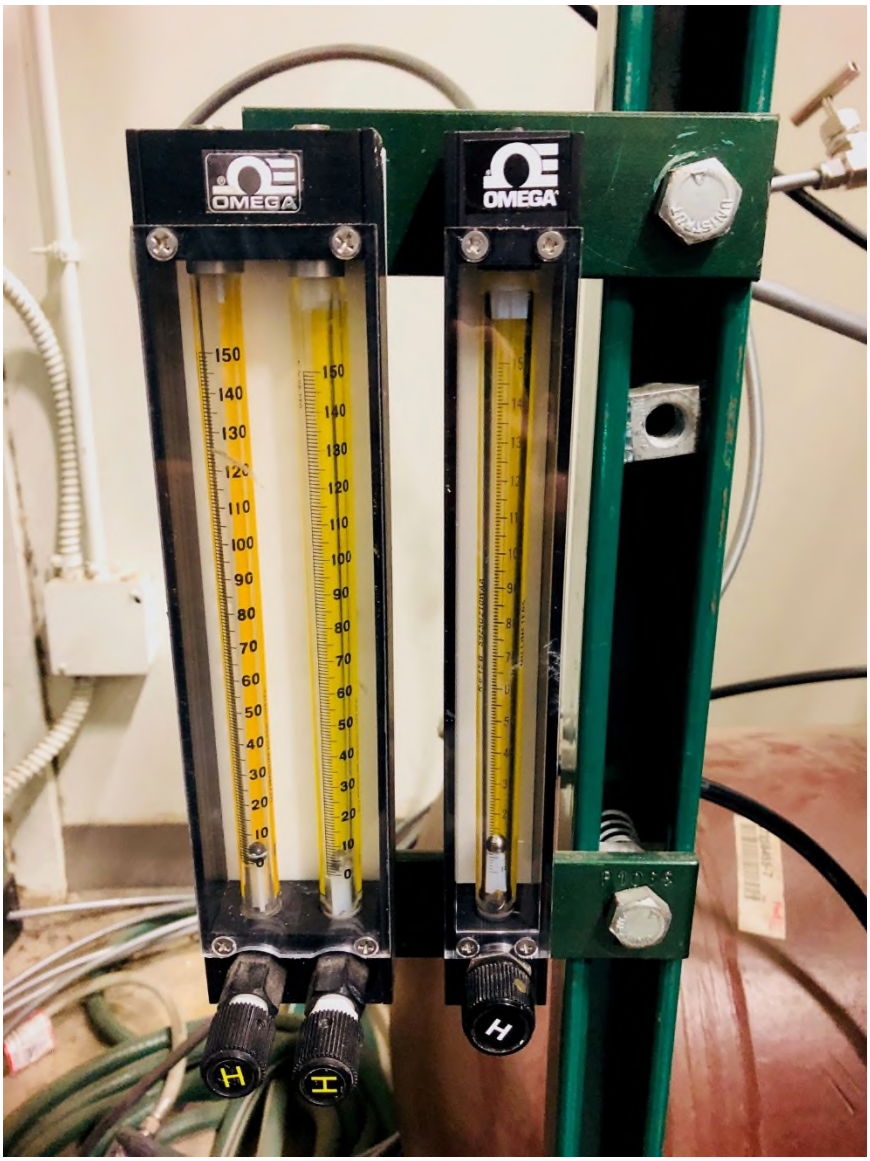

Figure 3.2a.7 – Rotameters used in parallel to achieve required flow rate capacity (Left: Note used, Middle: Omega Model: FL-1448-S, Right: Omega Model: 044-40-ST).

Figure 3.2a.8 – Pressure Control Valves (PCV-101) at Instrument Air Utility Supply Line.

Figure 3.2b.1 – Laser Control Tower (New Wave model: SOLO III PIV).

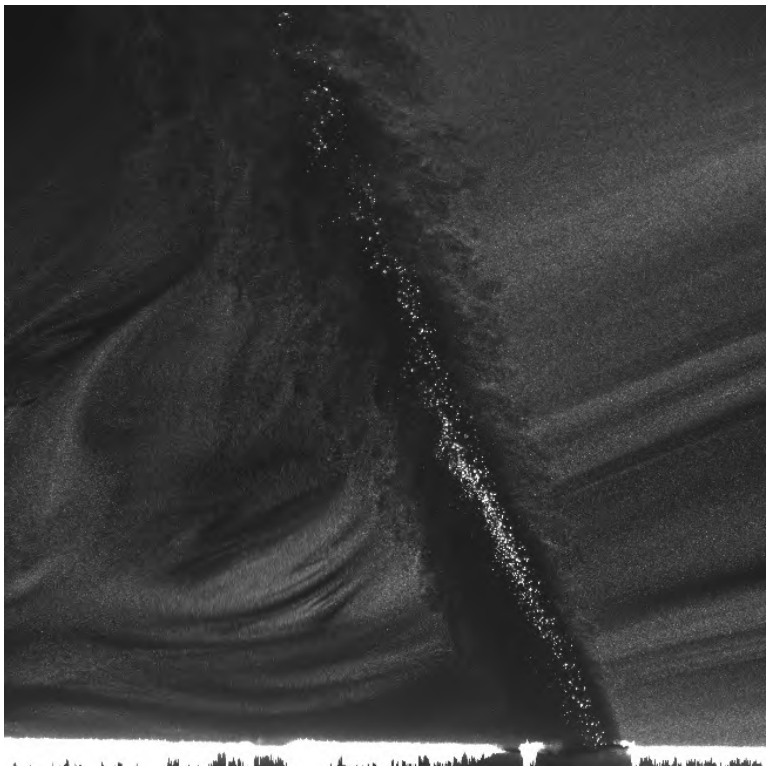

A

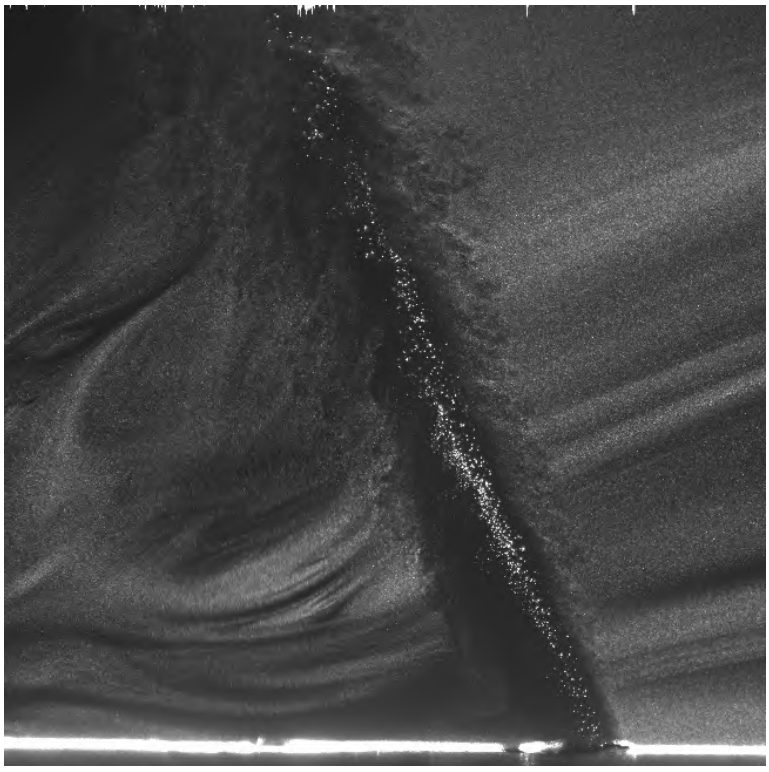

B

Figure 3.2b.2 – Image A (left) and Image B (right) of PIV captured imge pair.

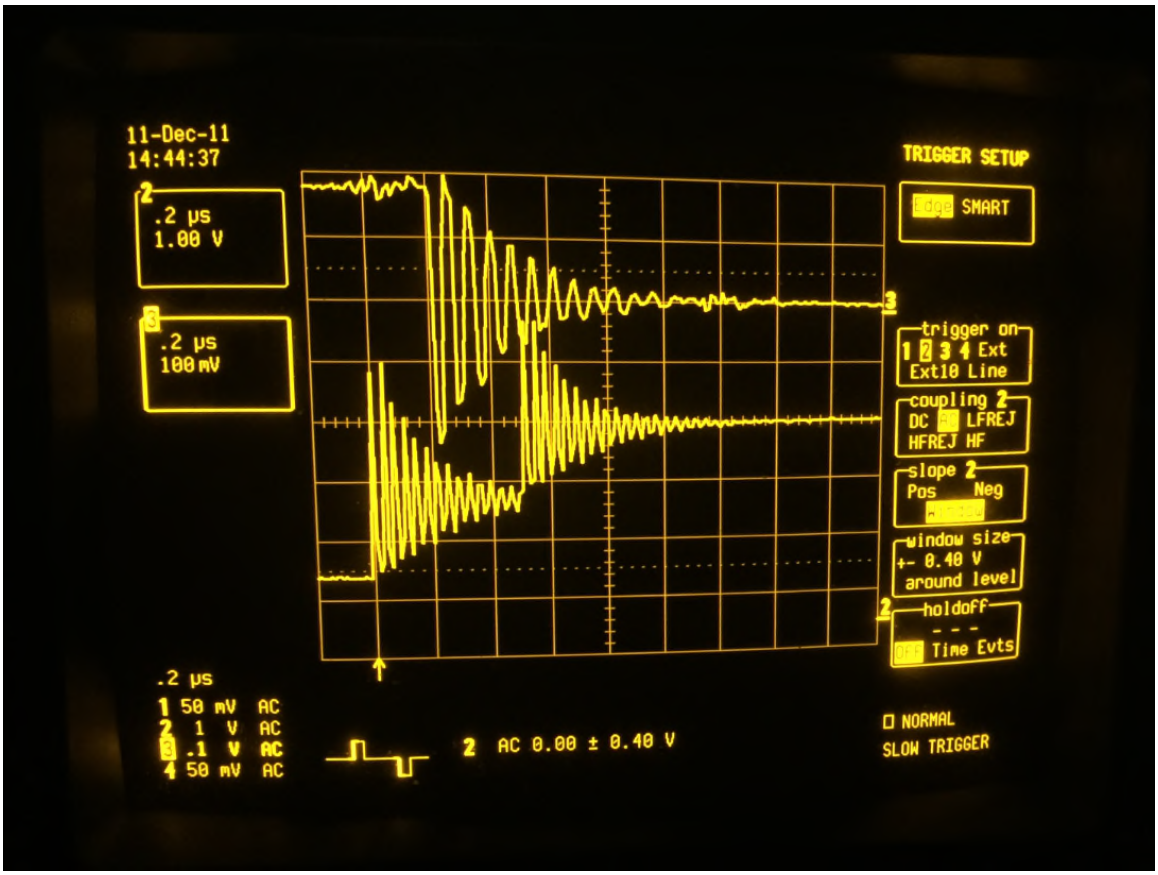

Figure 3.2b.3 – Two separate laser pulses indicated on either side of the camera trigger confirming pulse separation of 0.5 µs.

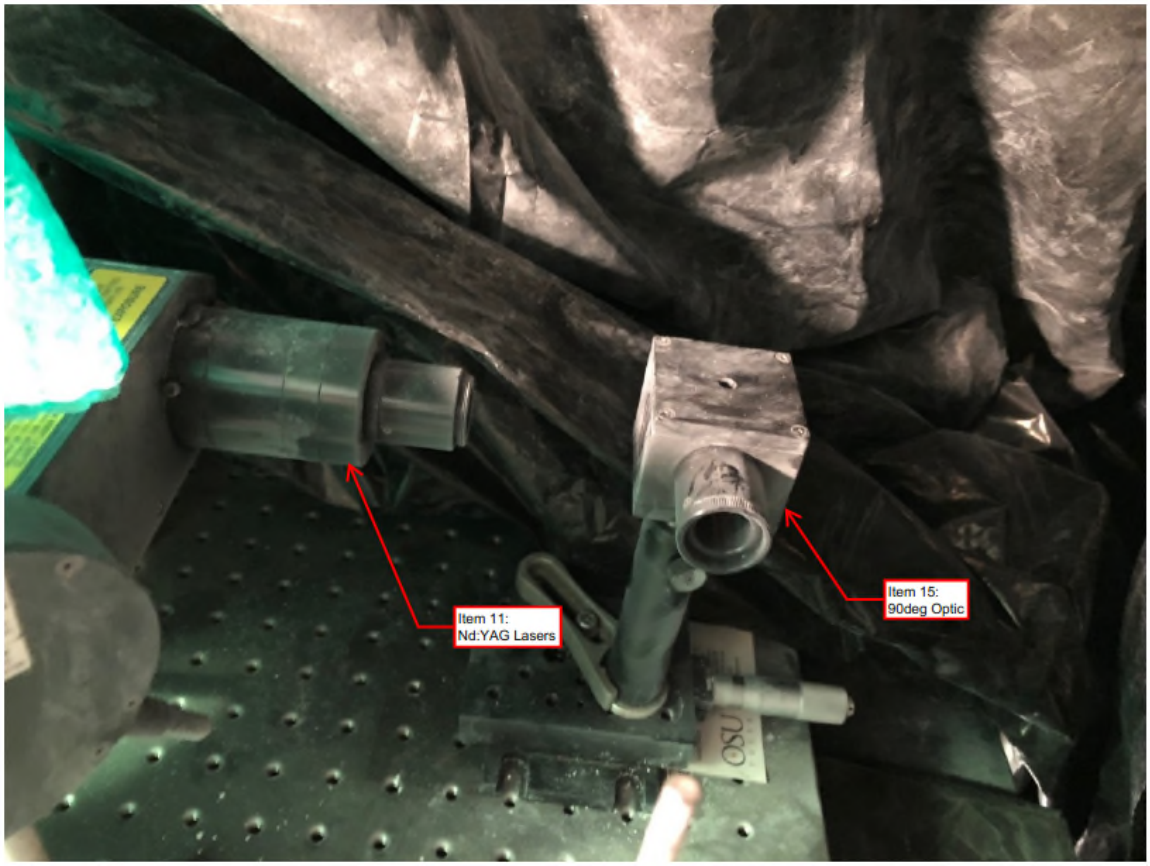

Figure 3.2b.4 – Laser discharge on left entering 90° mirror on right.

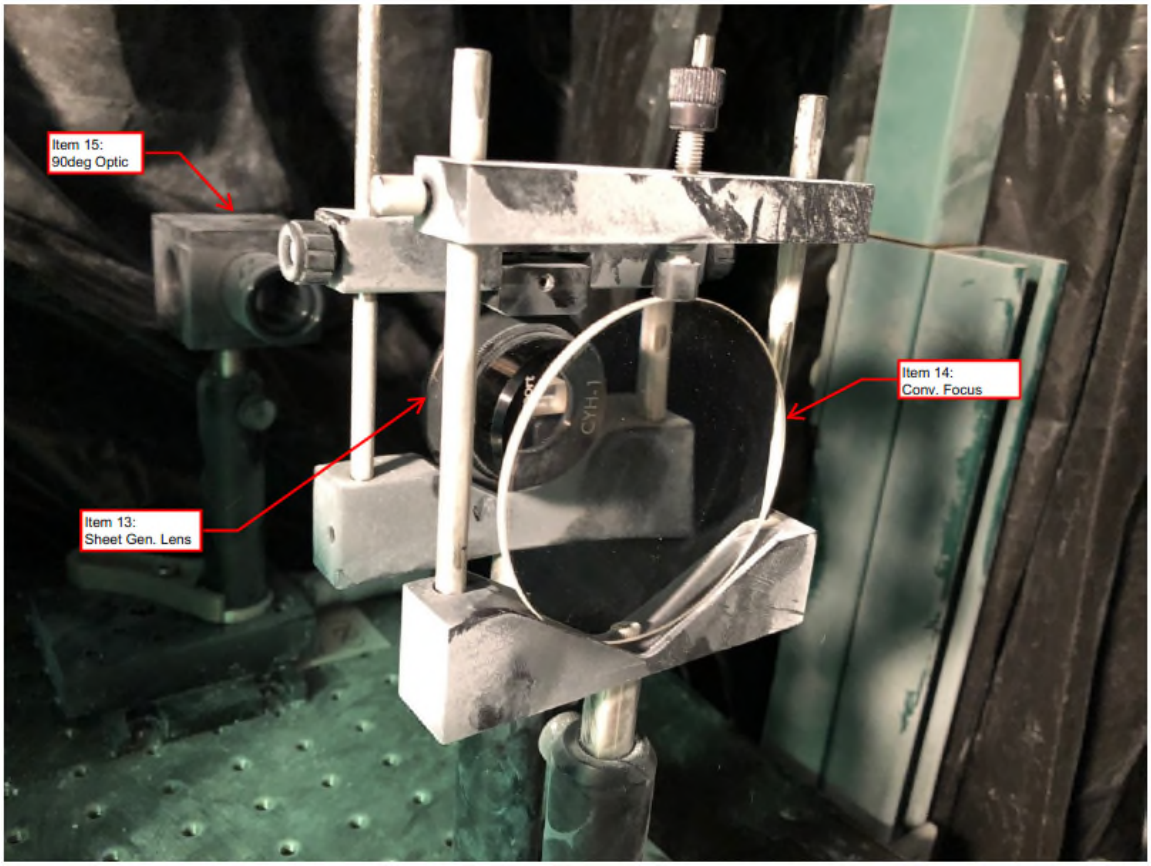

Figure 3.2b.5 – Cylindrical Lens (background) and spherical lens (foreground).

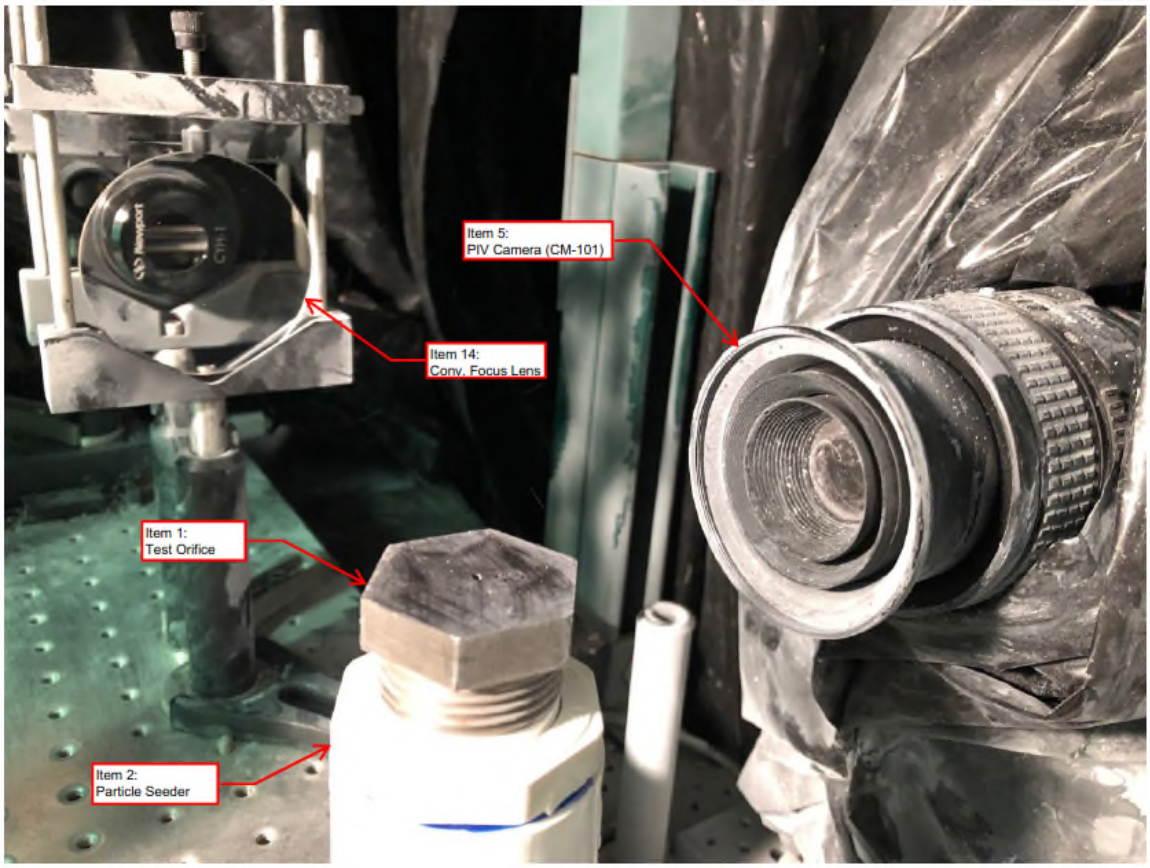

Figure 3.2b.6 – Laser Path and nozzle direction located perpendicular to camera lens.

Figure 3.2b.7 – Laser passing through each optical component with fog seeding of the entrainment environement and aluminum oxide particles exiting the test nozzle.

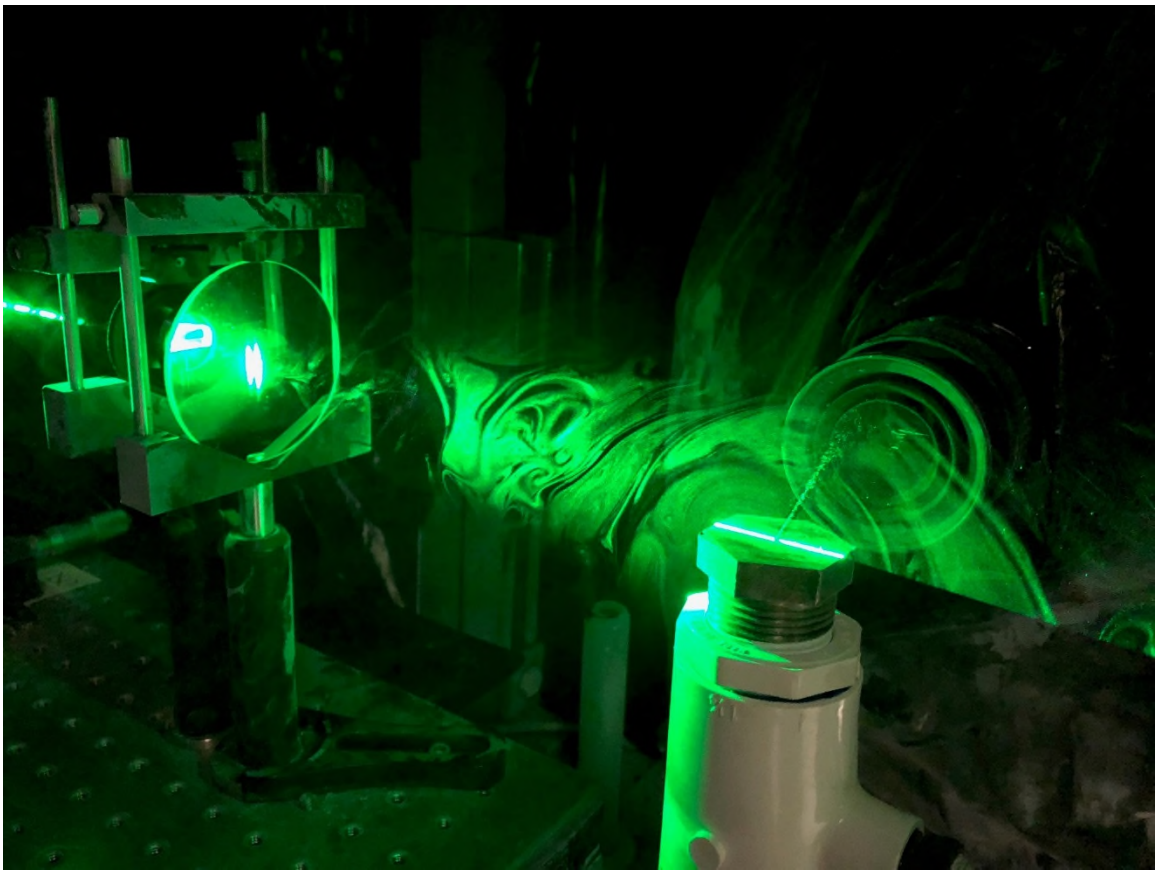

Figure 3.2b.8 – Laser pulse passing through 30° nozzle injection stream perpendicular to the camera lens

Figure 3.2c.1 – Camera (Model: PCO.2000, Cooled 14bit, 2048 x 2048 pixels).

Figure 3.2c.2 – Camera Lens (Nikon AF Micro Nikkor 60mm - 1:2.8 D).

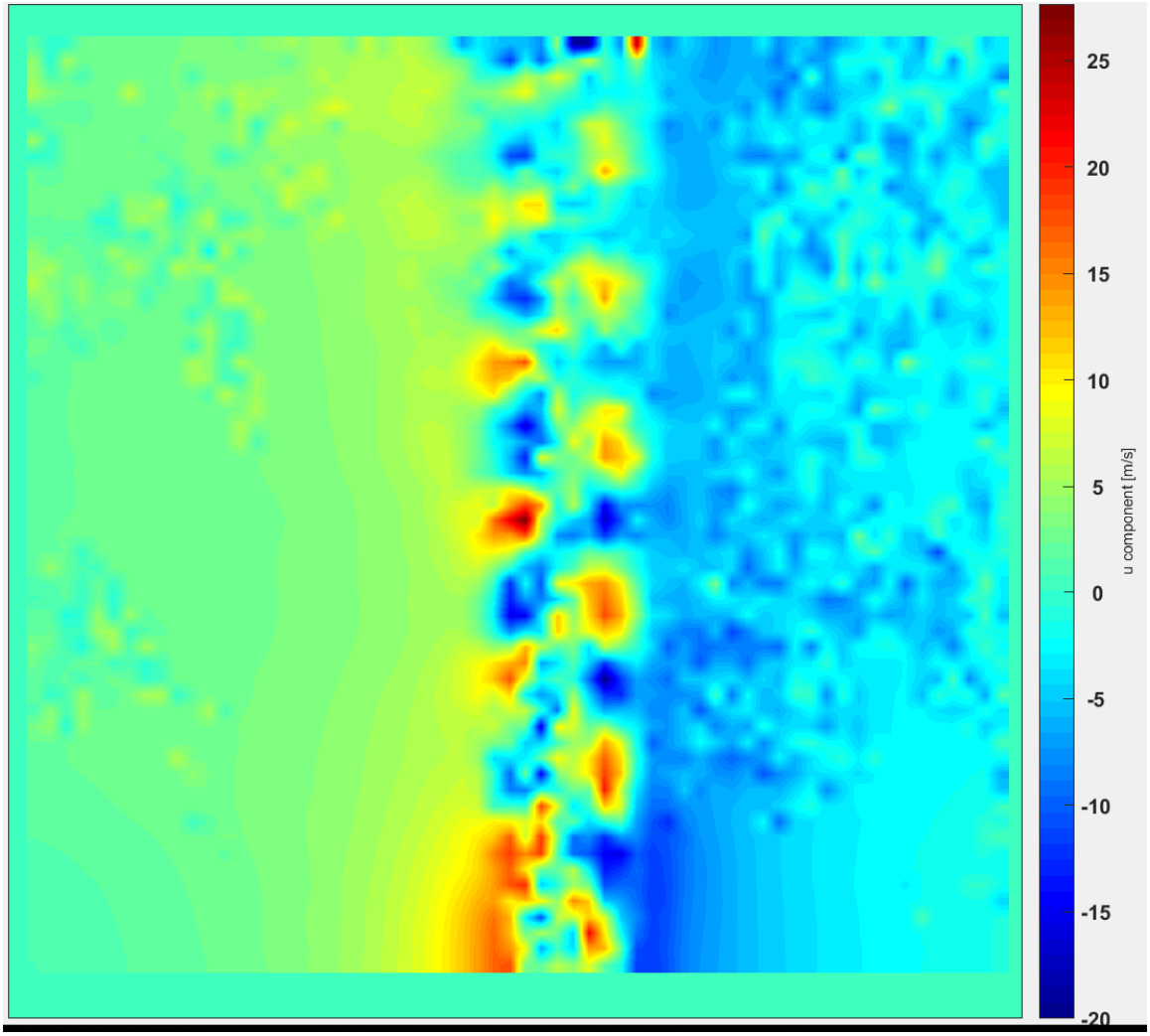

Figure 3.2c.3 - The average horizontal velocity components (u) of 125 image pairs for a vertical (0°) single choked jet nozzle.

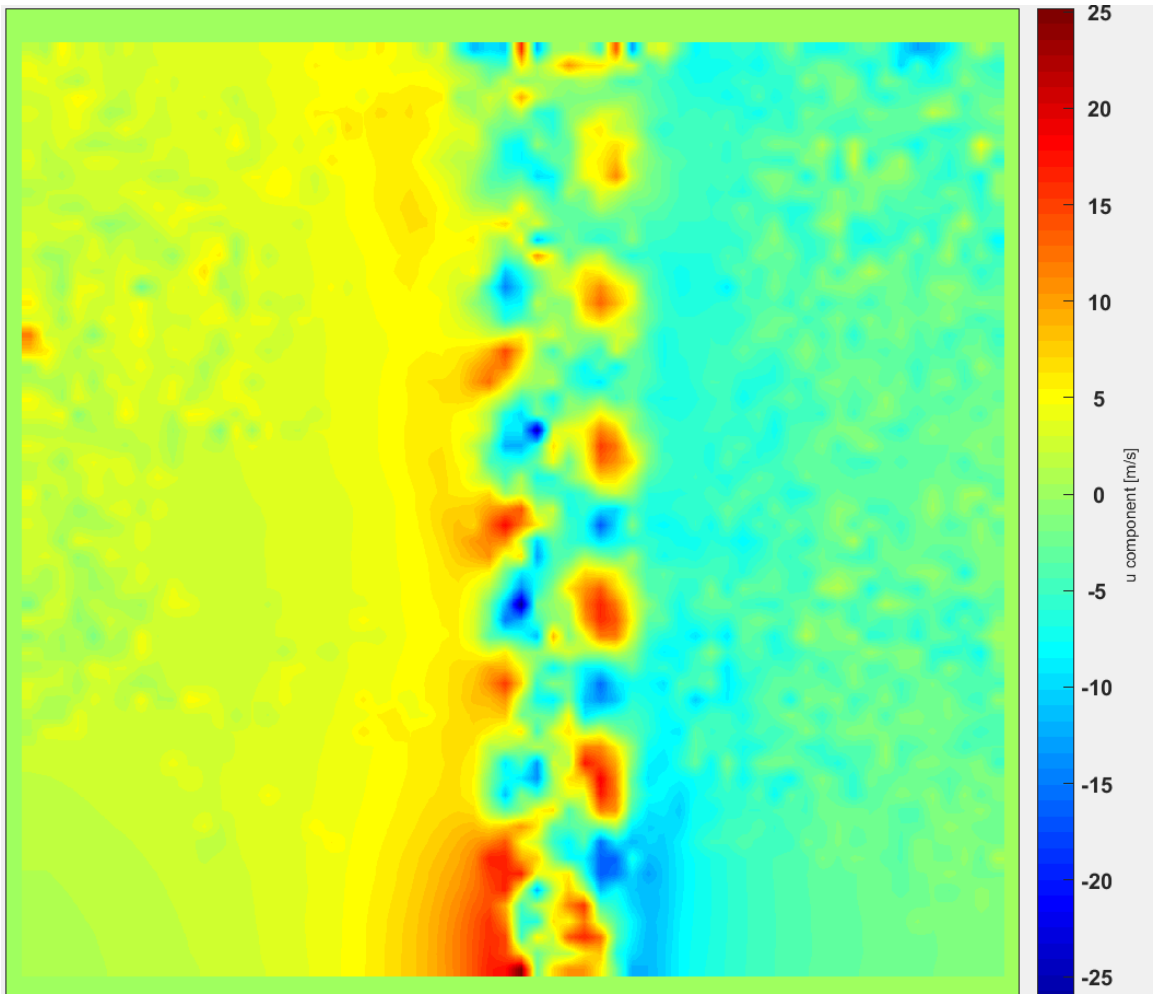

Figure 3.2c.4 - The average horizontal velocity components (u) of 250 image pairs for a vertical (0°) single choked jet nozzle.

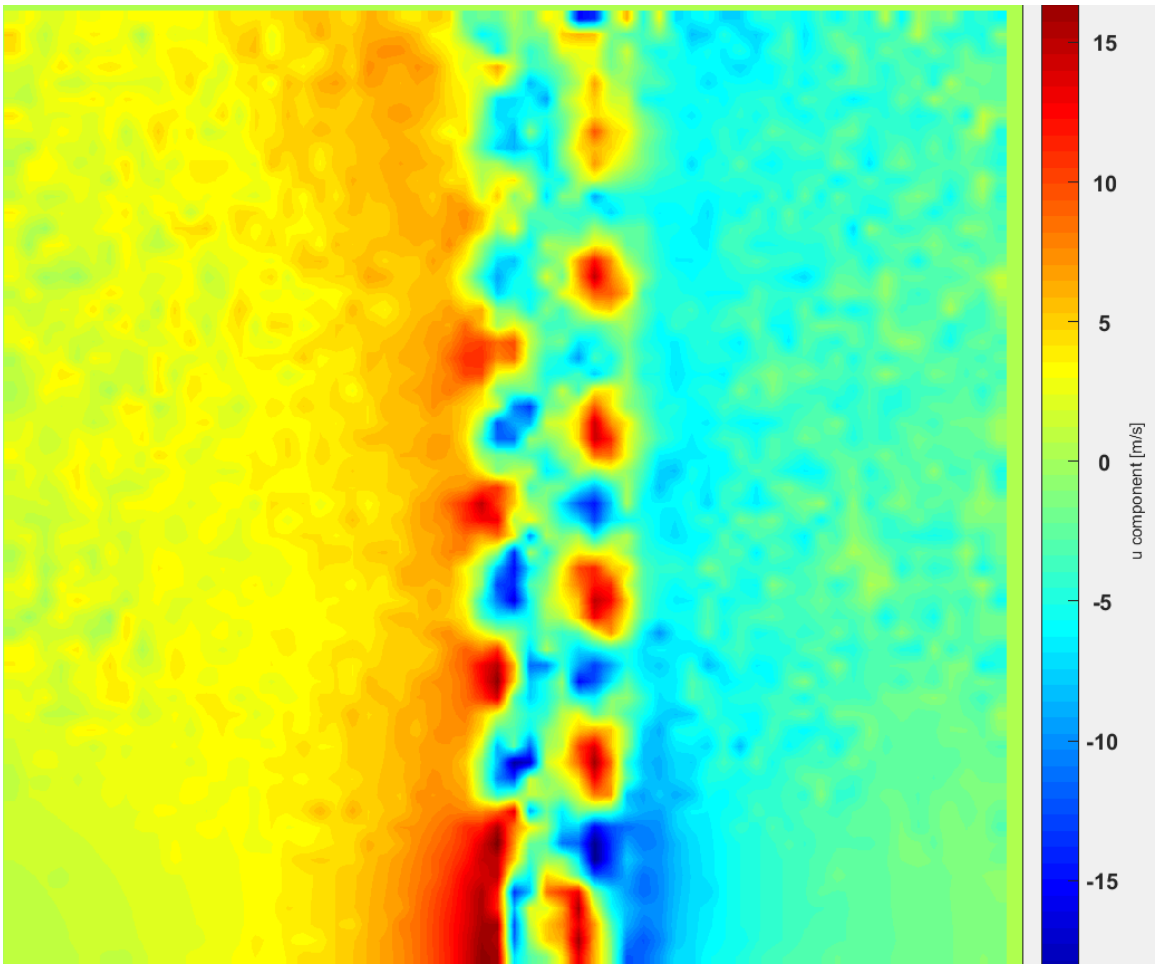

Figure 3.2c.5 - The average horizontal velocity components (u) of 500 image pairs for a vertical (0°) single choked jet nozzle.

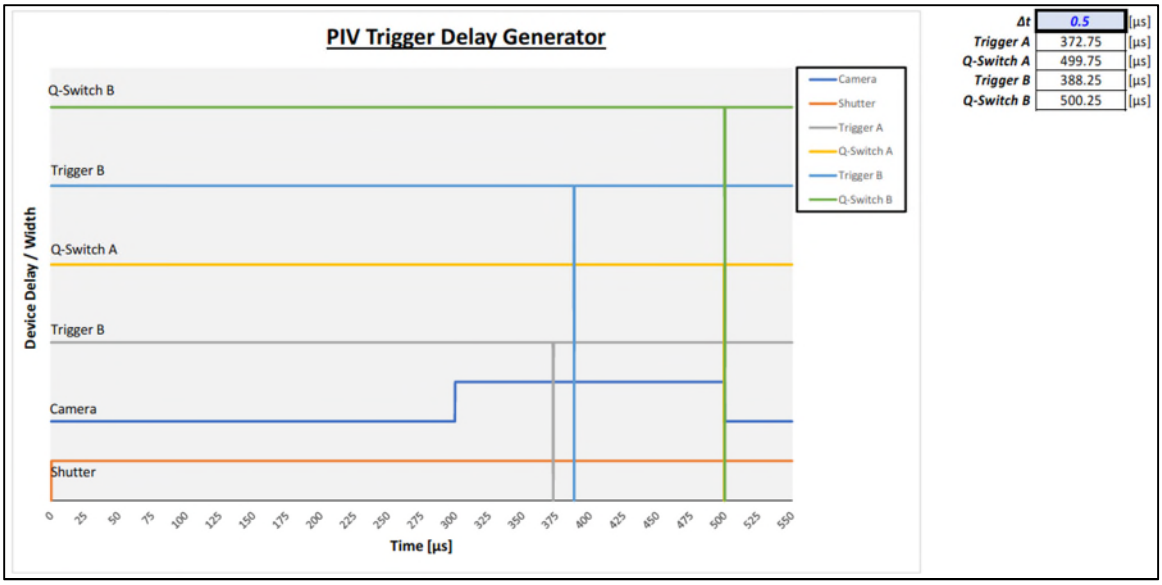

Figure 3.2c.6 - Depiction of delay generator trigger points. There is only a separation between the closure of the camera aperture and the Q-switch trigger of laser A & B of -0.25µs and +0.25µs respectively causing Q-switch A & B to appear as if they overlap each other in the graph.

Figure 3.3b.1 - Camera Calibration Target (Edmund Optics Model #: 38-710).

CHAPTER IV

RESULTS AND DISCUSSIONS

4.1 Introduction

This chapter presents experimental investigation of the flow field of inclined injection of choked jets and discusses the differences between normal and inclined injection. Computational results obtained by our collaborators are used to explain the experimental findings of the present study.

4.2 Achieving Choking Test Conditions

This section discusses the gas dynamics theory used to calculate the minimum chamber pressure (nozzle stagnation pressure) required to achieve choked flow condition from the tested axisymmetric orifices. The gas dynamics theory is capable of calculating the theoretical volumetric flow rate through the orifice at the present test conditions, the expansion fan angles, the Mach disk locations, and the nozzle exit velocity.

4.2a Chamber Pressure

In this study, the back pressure [$Pamb$] is atmospheric and is relatively constant at 14.32 psig using the hypsometric equation:

$$P_{amb} = 14.7\left(1 - \frac{0.0065h}{T+0.0065h+273.15)}\right)^{5.257} \quad (4.2a.1)$$

where h is the elevation from sea level in meters for Tulsa, Oklahoma, and T is the temperature in °C at standard conditions. For isentropic flow through the orifice the following equation is used to determine the minimum chamber pressure (P_o) required to achieve choked flow through an orifice:

$$\frac{P_{amb}}{P_o} = \left(\frac{2}{k+1}\right)^{\left(\frac{k}{k-1}\right)} \tag{4.2a.2}$$

where P_o is the chamber pressure, P_{amb} is the downstream pressure from the nozzle exit, and k is the specific heat ratio for air. In this application air is assumed as an ideal gas having a specific heat ratio (k) value of 1.40. Applying the known k value for air to equation 4.2a.2 the following equation can be used to calculate the minimum chamber pressure (P_o) required at the nozzle chamber to achieve choked flow (M ≥ 1.0)

$$P_o = \frac{P_{amb}}{0.5283} \tag{4.2a.3}$$

Using equation 4.2a.3 it was calculated that a theoretical minimum P_o of 27.8 psia is required to achieve choked flow through an orifice into a downstream environment at atmospheric pressure. This is the minimum allowable value throughout data collection session for P_o (*indicated by pressure gauge PG-201*) to achieve choked flow.

4.3 External Flow

A typical flow visualization for each of the test nozzles can be seen in Figure 4.3.1a. Of interest is the path of the seeding particles injected from the nozzles. In the inclined injection case the particles seem to prefer the right hand side of the nozzles. The reason for this preference will be explained later in this chapter.

4.3a Normal Injection (0°)

A test nozzle with an injection angle of 0° was used as a control and to confirm that the experimental results aligned well with the expected characteristics of an under-expanded jet. General gas dynamic theory [John and Keith, 2006] provides the theoretical prediction of shock diamond geometry produced by an under-expanded gas jet (Figure 4.3.1).

For the 0° test nozzle the flow was found to be axisymmetric as expected for an under-expanded jet. Clear indication of this axisymmetric geometry was observed in the evaluation of the vertical and horizontal velocity components of the flow (Figures 4.3.5a and 4.3.5b). Figure 4.3.5b shows clear indication of the axisymmetric shock diamond structure produced by the flow. The experimental results indicated a maximum achieved Mach number of M = ~1.3 (450m/s) in the vertical direction (Figure 4.3.5a) which aligned with theoretical expectation. The Mach diamonds were shown to decay as the pressure equalizes with atmospheric pressure (P_amb) due to the dissipative nature of the oblique shock waves. The experimental results for the 0° nozzle agreed with the expected flow characteristics and shock diamond geometry well (Figures 4.3.5a/b). These results provided validation of the present experimental methods and were used as a control for the remainder of the experimental data collection process.

It was also confirmed that the vent hood used in the experimental set up did not adversely affect the entertainment flow and it did not introduce an external source of kinetic energy (draft) to the particles in the entrainment field (see Section 3.2b for procedure). Figures 4.3.4a/b/c show that for all three test nozzles the entrainment particle velocities were observed moving in the horizontal direction until coming in contract with the free jet boundary. This assured us that the flow field was not affected by any draft introduced by the vent hood.

4.3b Inclined Injection (15°) and (30°)

Sectional views of the 0° control nozzle and the two experimental nozzles with titled injection axes at 15° and 30° are shown in Figure 3.2.1. After the investigation of the 0° control nozzle found that the experimental results agreed with the theoretical flow characteristic for an under-expanded choked jet, the 15° and 30° experimental nozzles were investigated next. The flow visualizations for these two test nozzles can be seen in Figures 4.3.2a and 4.3.2b.

It can be seen through visual inspection of these images that the solid seeding particles embedded in the injection flow are not symmetrically distributed within the main body of the jet but rather have preferentially migrated to the right edge of the jet. Close attention was paid to the design of the particle seeder to ensure that the seeding particles were uniformly distributed throughout the pressure chamber prior to exiting the test nozzles. The nozzles were manufactured with high precision by a 5-axis CNC machine and inspected post-production for any defects or burring that could adversely affecting the test results due to non-symmetric nozzle geometry. The nozzles were also inspected visually during the testing phase for blockage. No blockages were observed. Due to these careful design considerations it was surprising to see clear indication of a flow structure that was not symmetric about the jet's axis.

Further confirmation of this non-symmetric flow was confirmed when the velocity magnitudes where evaluated in the vertical and horizontal directions with respect to the injection angles. Figure 4.3.6 shows the experimental velocity magnitude results in the vertical direction with respect to the injection angle for the 15° nozzle. The maximum velocity magnitudes have migrated outward toward the right edge of the jet confirming the observed path of the seeding particles. Figure 4.3.7 shows the velocity components in the direction normal to the injection axis of the nozzle and further provides confirmation of this non-symmetric flow behavior by the 15° test nozzle.

Figures 4.3.8 and 4.3.9 show the velocity magnitude results for the 30° nozzle in the vertical and horizontal directions respectively. These results show that the 15° results were not an anomaly but instead confirm that the peak velocity magnitude of the jet tend to be more asymmetric as the angle of the jet is increased. The 30° velocity magnitude results show that in the direction normal to the injection axis the velocity on the right-hand side of the jet are substantially larger than the corresponding left-hand velocities by approximately two to two-half times.

The average vorticity fields for each of the three test nozzles were also measured (Figures 4.3.5.b, 4.3.8, and 4.3.11). These results also confirmed that the inclined jets were not symmetric across their axes. It was also confirmed that this phenomenon increased in severity as the angle of the jet increased. It can be speculated that this asymmetric flow pattern produced by the angled jets could be due to an asymmetric expansion wave triggered at the nozzle's exit. It could be assumed that the expansion fan triggered at the right edge of the nozzle's exit has a larger share of the injection exit flow area compared to the wave triggered at the left edge since both expansion fans should have the same fan angle given by [John and Keith, 2006]:

$$\varphi = \mu_1 - \mu_2 + \Delta \tag{4.3.1}$$

where the turning of the flow is based on the pressure ratio of the back pressure (Pamb) and the nozzle exit pressure, P*. As a result of the uneven expansion fan angles between the left and right-hand sides of the nozzle exit, most of the jet flow is attracted outward (to the right). Further downstream, as the shock waves are triggered the Mach diamonds would gradually dissipates unsymmetrically. Having a flow region dominated by a right edge expansion fan could explain the asymmetric flow, but this reasoning does not explain the "long neck" region observed on the left side of the jet near the nozzle exit (Figure 4.3.9), nor does it explain the reason the seeding particles were injected with a preference toward the right-hand side of the nozzle. The "long neck" region observed on the left hand side may cause an observer to conclude that the nozzle was partially

obstructed during testing. This conclusion could be further bolstered when considered alongside the observation that most of the seeding particles appear to leave the nozzle on the right-hand side. However, the nozzle was not obstructed in any way throughout testing.

4.4 Internal Flow

It was concluded that there was a need to inspect the flow field inside the injection port (internal flow) to explain the seeding particles trajectories as well as the "long neck" region on the left-hand side. Another computational study [Sheridan et al., 2019] was initiated as a result by our collaborators. The computational results are included in this section (4.4) for completeness.

The simulation of the internal flow characteristics of each of the three test nozzles was performed using STAR-CCM+ CFD software (currently owned by Siemens). This analysis was critical in explaining the asymmetric flow characteristics and "long neck" anomaly of the two inclined nozzles. When the results of the CFD simulations were compared to the experimental results presented in Section 4.3 they were found to be in very close agreement with each other. This served as a further validation of the techniques implemented during both simulation and experimental data collection.

The computational velocity magnitude results for the 15° nozzle are shown in Figures 4.3.12a and b. The results shown in Figure 4.3.12a confirm right-hand flow dominating expansion waves. In addition, when evaluation of the nozzle was rotated to a perspective inline with the nozzle exit direction (Figure 4.3.12b) the symmetry of the expansion wave triggering was, as expected, confirmed in the two directions normal to the injection plane. However, the structure of the internal nozzle flow was surprising. Figure 4.3.13 demonstrates an internal nozzle flow dominated by an embedded expansion fan

triggered at the lower left edge of the port as the flow direction changes when entering the nozzle's throat. On the right hand side, however, the flow was gradually introduced into the port and no pressure drop was observed. As a result, the majority of the flow velocity entering the injection port is preferentially driven to the right side of the port due to the triggered expansion fan within the nozzle. This internal flow pattern explains why the majority of the seeding particles were observed exiting the nozzle along the right side of the jet [Figure 4.3.2c] and helps to further explain the reasoning for the "long neck" anomaly observed in Figure 4.3.9 being that the flow velocity was so much lower on the left-hand side when exiting the nozzle.

Computationally generated "Schlieren images" where created by our collaborators [Sheridan et al., 2019] by plotting the density gradient to further investigate the internal flow characteristics of the inclined jets. Figures 4.3.15 and 4.3.16 show the results of this evaluation and provide a good visual depiction of the wave structure for both internal and external flows to the test nozzles. These results clearly mark the expansion fan angles at both the nozzle inlet and exit as well as the existence of a slip plane within the port.

The computational "Schlieren imaging" and the computational internal velocity magnitude results generated by the CFD analysis brought forth a new question of why an asymmetric wave trigger was being produced at the left-hand side of the inlet to the port's throat. Figure 4.3.14 is a computational representation of the pressure distribution inside the nozzle [Sheridan et al., 2019]. The figure shows that there is very little pressure change at the right-hand side of the port's inlet indicating graduate velocity change on that side. However, on the left-hand side of the port's inlet there is clear indication of pressure reduction at the inlet. Due to the nature of the converging flow approaching the nozzle

inlet, there is a rapid turning of the flow direction at the left side of the port resulting in the triggering of an expansion fan. On the right side of the inlet, however, there is a very minor change in flow direction resulting in very little change in pressure. As further confirmation of these conclusion, the velocity magnitude profiles for the left and right-hand sides of the nozzle inlet can be seen in Figure 4.3.13. A slip plane exists within the injection port which separate two regions with the same pressure but different velocities. A large flow velocity region exists to the right where the majority of the seeding particles are moving and a slow (almost stagnant) region exits on the left-hand side of the port.

Figured 4.3.13, 15, and 16 each show clear indication of supersonic flow within what many would consider to be a converging-only nozzle. Theoretically a converging-diverging (de Laval) nozzle is required to generate supersonic flow inside of a port prior to exiting. However, in the present study it has been shown that inclined injection can create a fluidic converging-diverging nozzle resulting in supersonic exit velocities from a simple inclined round orifice. Figure 4.3.17 shows a diagram of the wave structure for a nozzle. having a sharp edge entrance being injected into a quiescent environment at an angle.

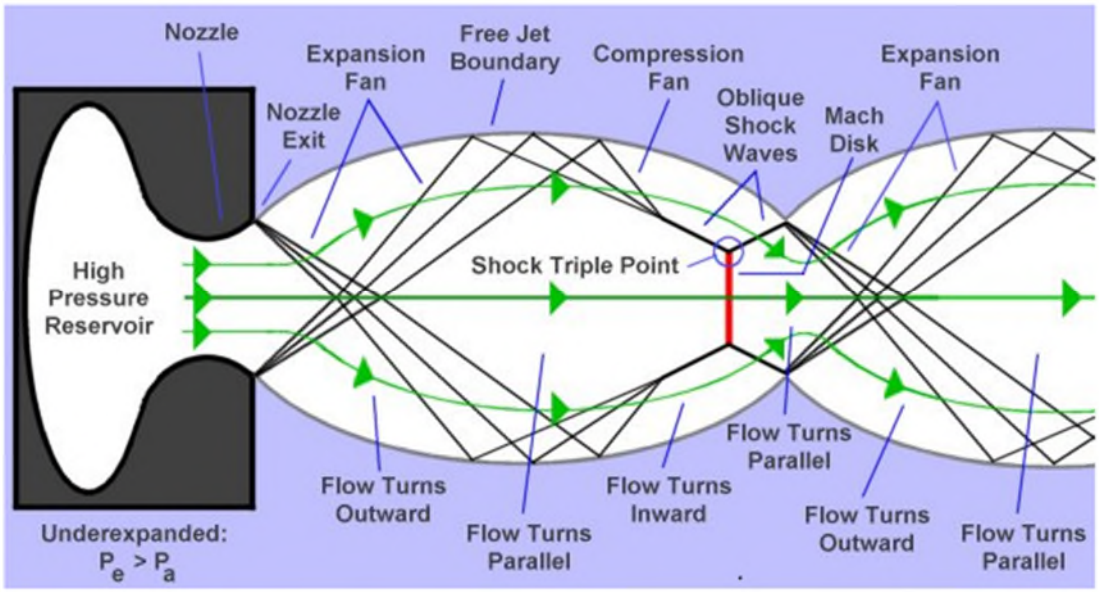

FIGURE 4.3.1 The wave structure of under-expanded jet (Source: http://www.aerospaceweb.org) injected normally in a quiescent environment.

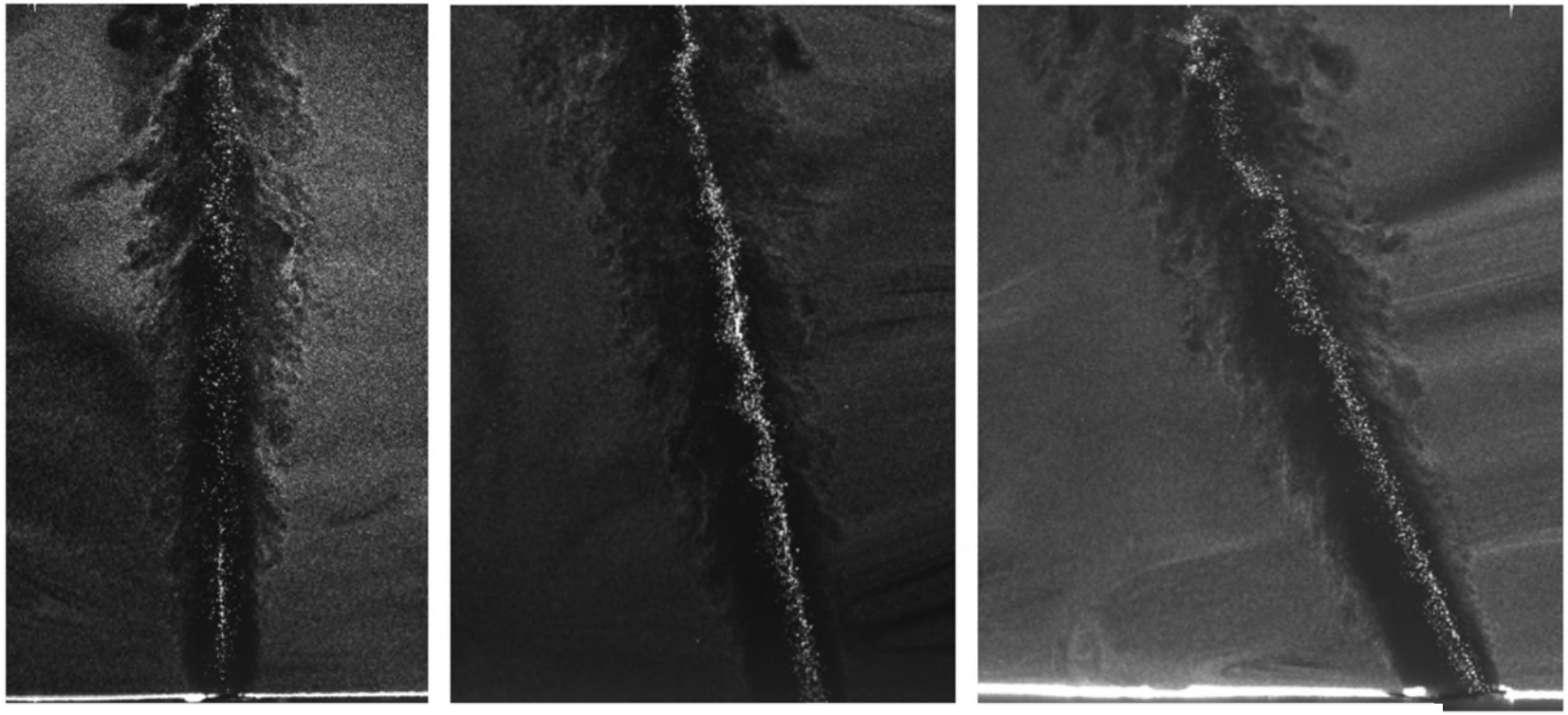

A **B** **C**

FIGURE 4.3.2 Inner and outer seeding of choked gaseous jets: a) Normal injection, b) 15^{o} injection, and c) 30^{o} injection.

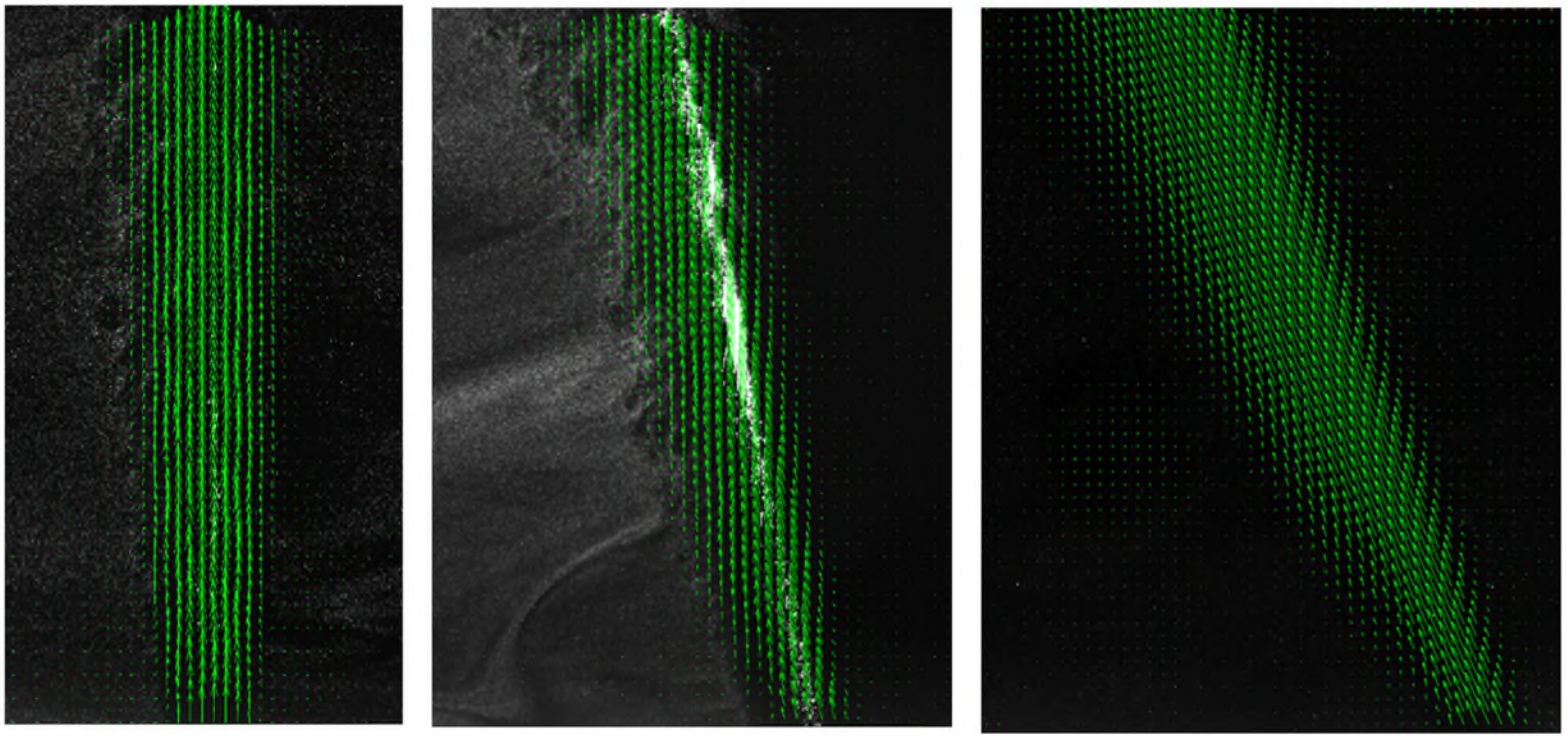

A **B** **C**

FIGURE 4.3.3 Velocity vectors of choked gaseous jets: a) Normal injection, b) 15^{o} injection, and c) 30^{o} injection.

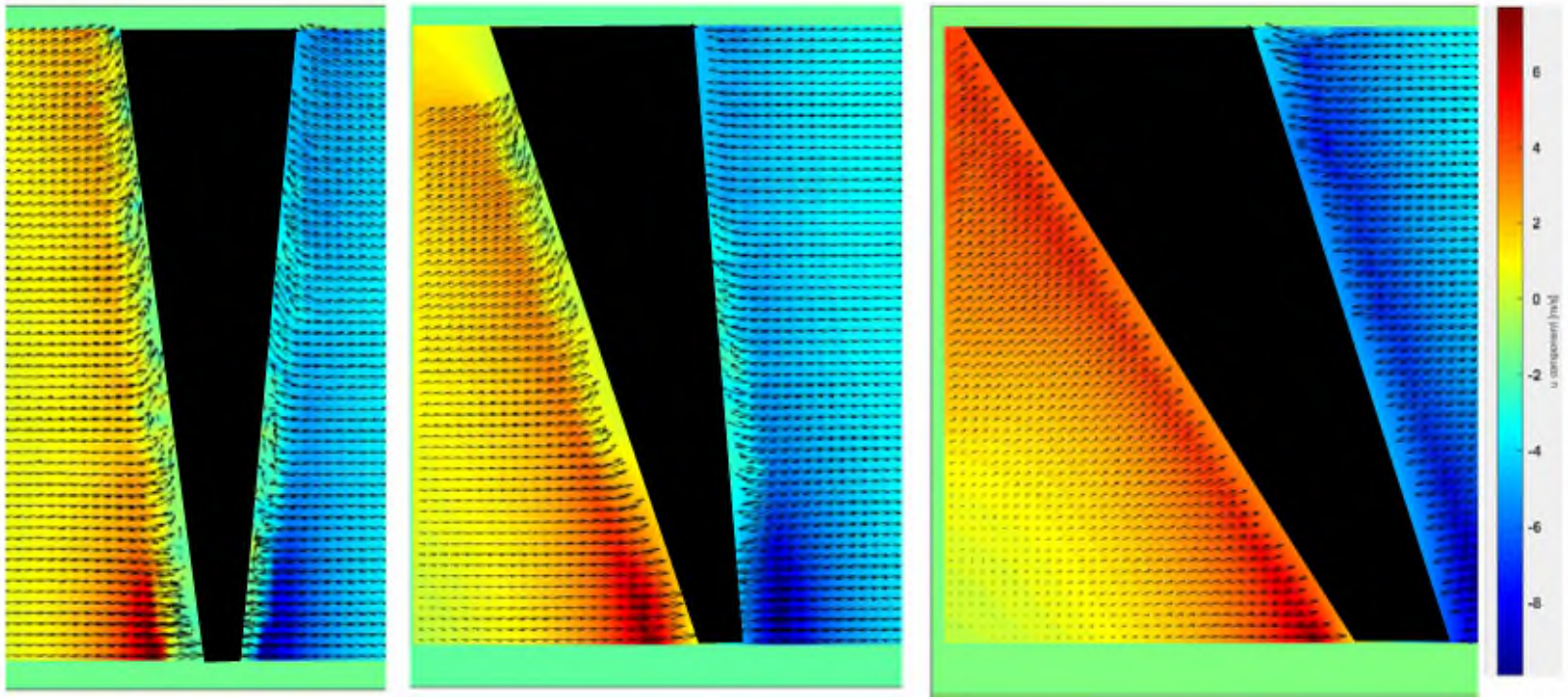

FIGURE 4.3.4 Velocity field of the entrainment flow. The figures are colored by the horizontal velocity magnitude for choked gaseous jets: a) Normal injection, b) 15^{o} injection, and c) 30^{o} injection.

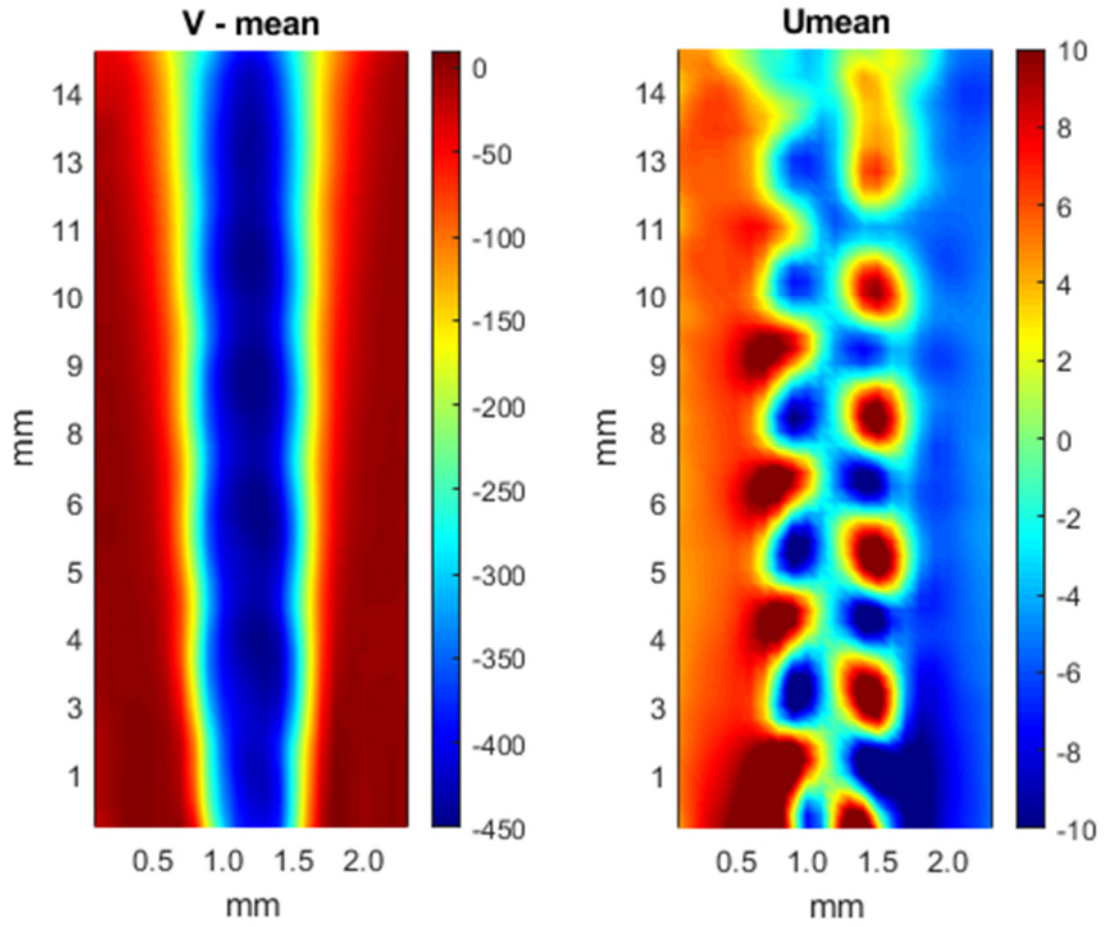

(a) (b)

FIGURE 4.3.5 Experimental (a) vertical and (b) horizontal velocity components of normal injection of choked gas jet. The alternating horizontal velocity components indicate the presence of symmetric shock diamonds. Negative vertical velocity indicates upward flow direction.

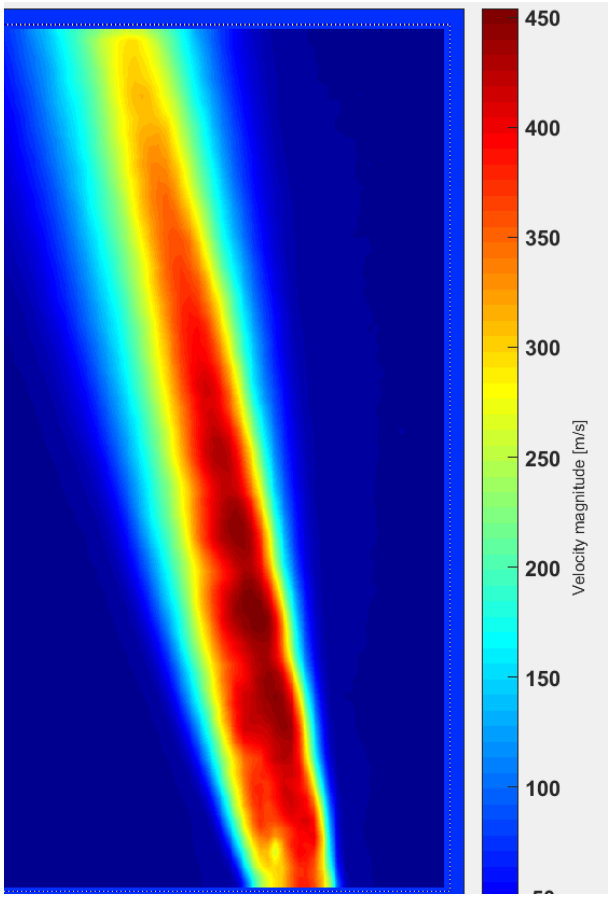

FIGURE 4.3.6 Experimental velocity magnitude of an inclined (15°) choked gas jet.

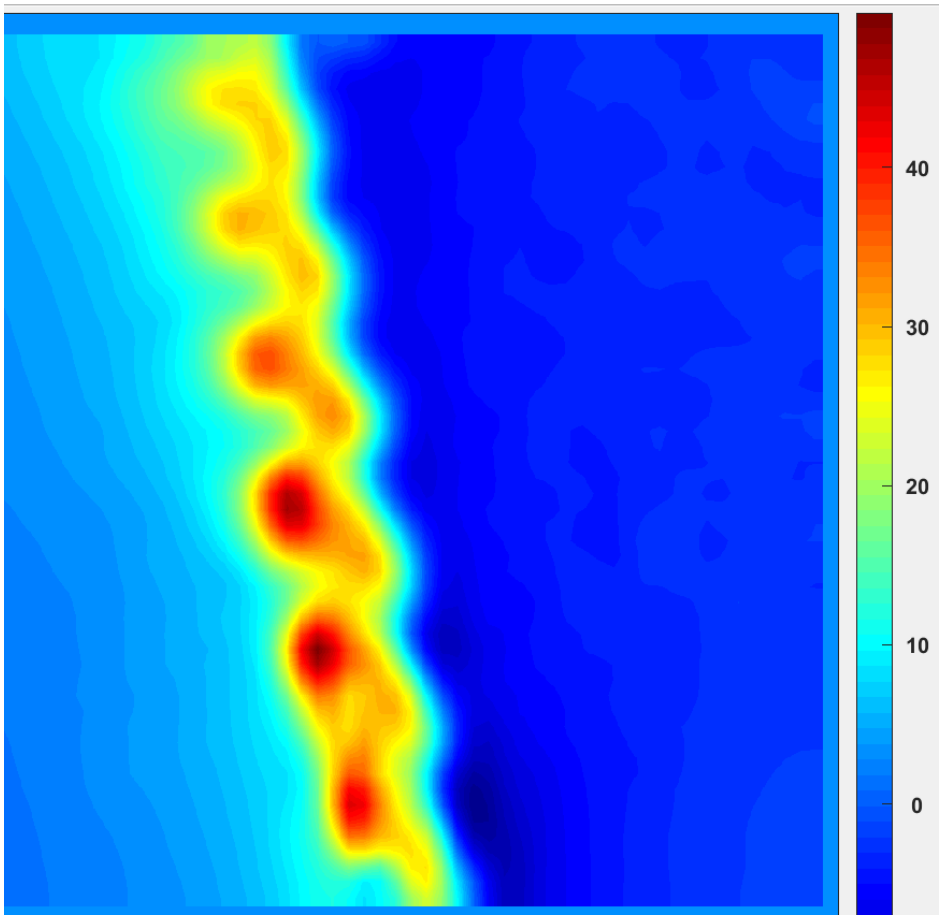

FIGURE 4.3.7 Experimental velocity component (m/s) normal to the injection direction of an inclined (15°) choked gas jet.

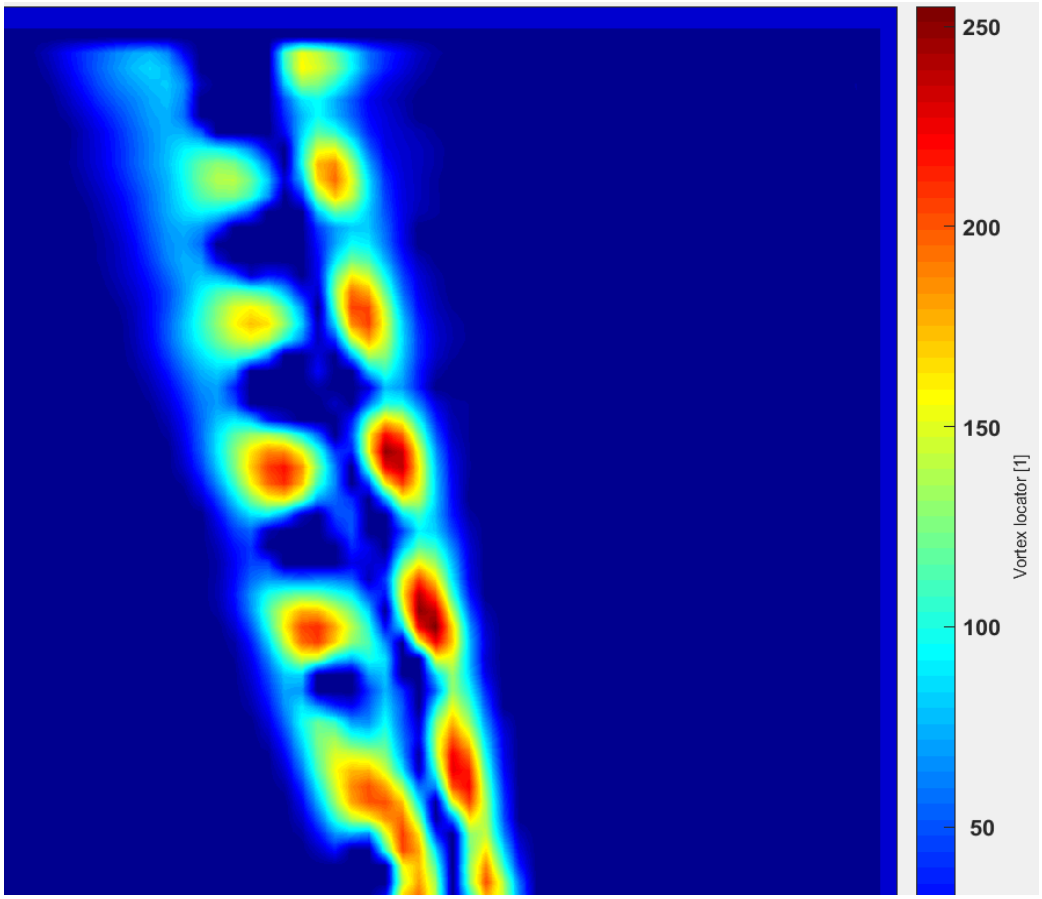

FIGURE 4.3.8 Experimental vortex locator of an inclined (15^{o}) choked gas jet.

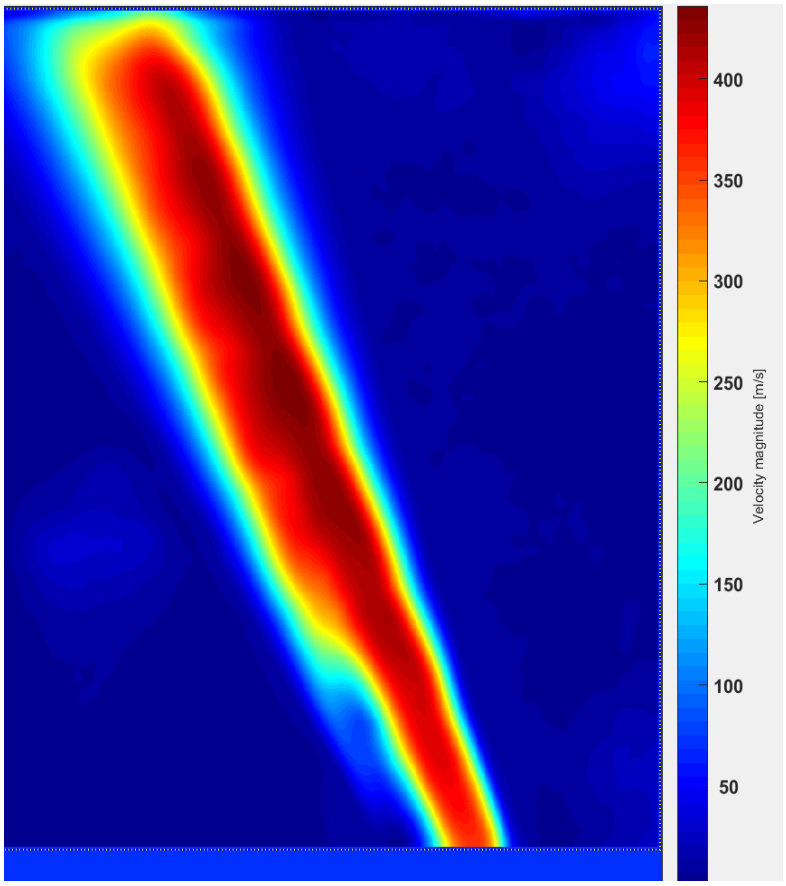

FIGURE 4.3.9 Experimental velocity magnitude of an inclined (30°) choked gas jet.

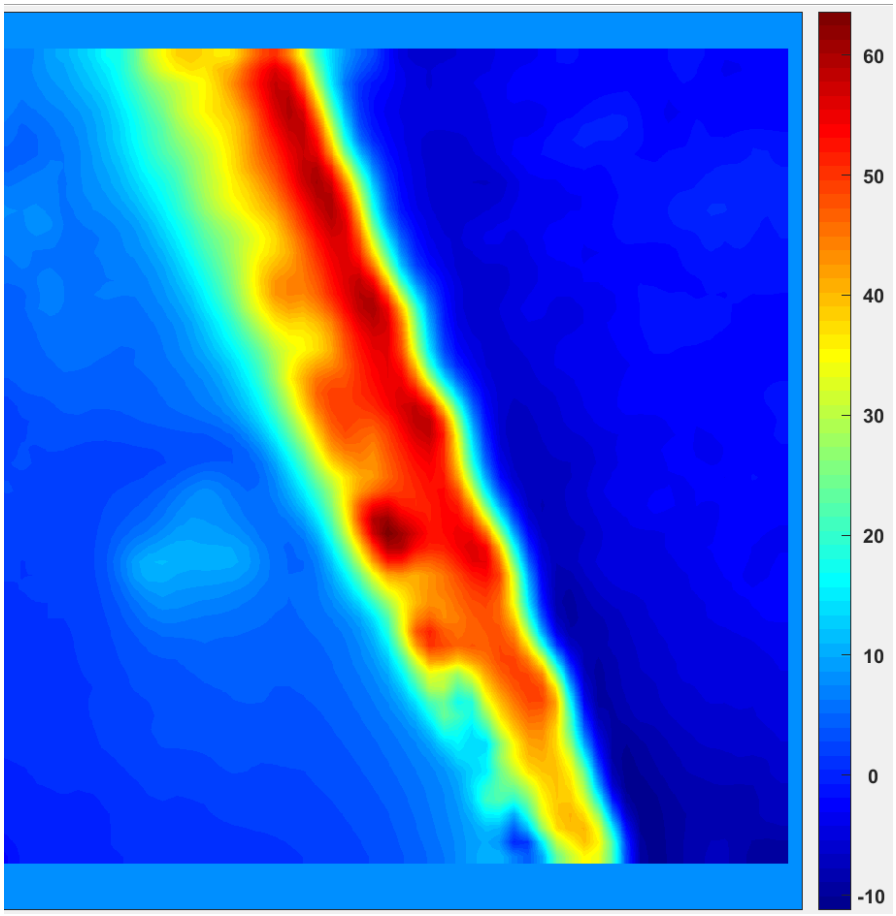

FIGURE 4.3.10 Experimental velocity component (m/s) normal to the injection direction of an inclined (30°) choked gas jet.

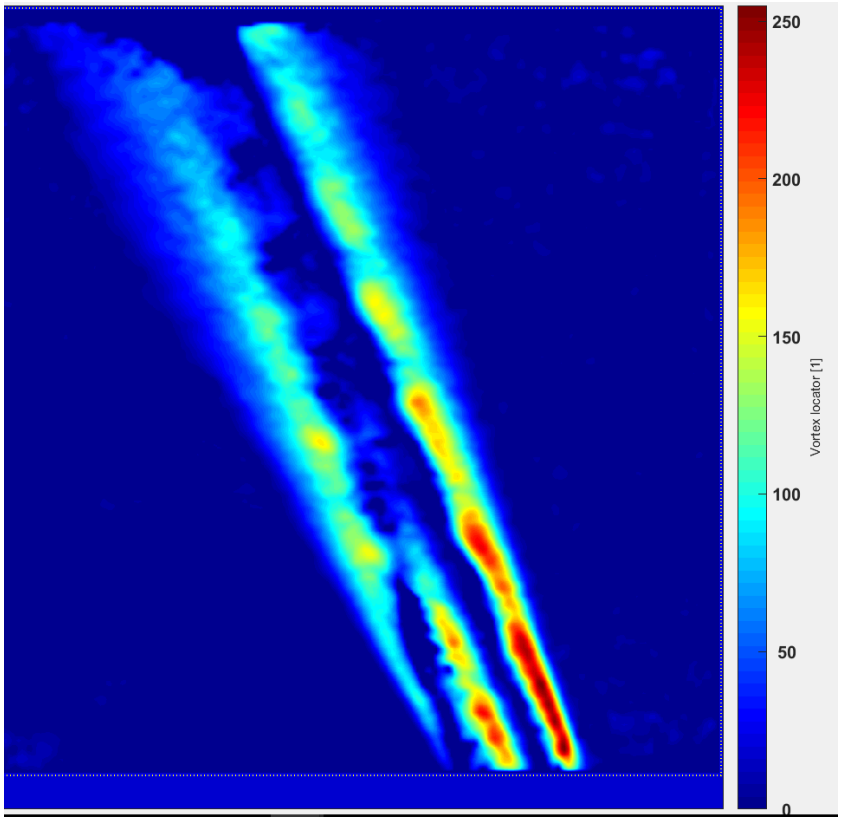

FIGURE 4.3.11 Experimental vortex locator of an inclined (30º) choked gas jet.

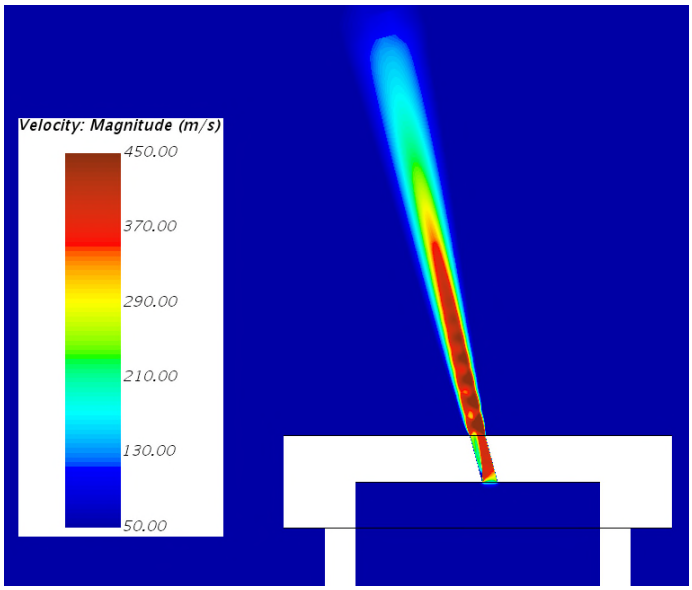

A

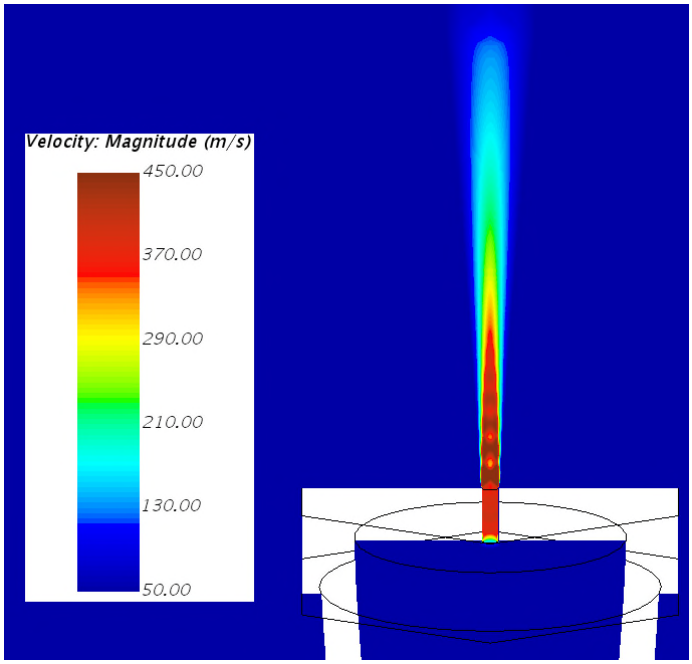

B

FIGURE 4.3.12 Computational velocity contours for choked inclined (15°) gas jet (A) Side view, (B) normal to injection plane view (Source: Sheridan et al., 2019).

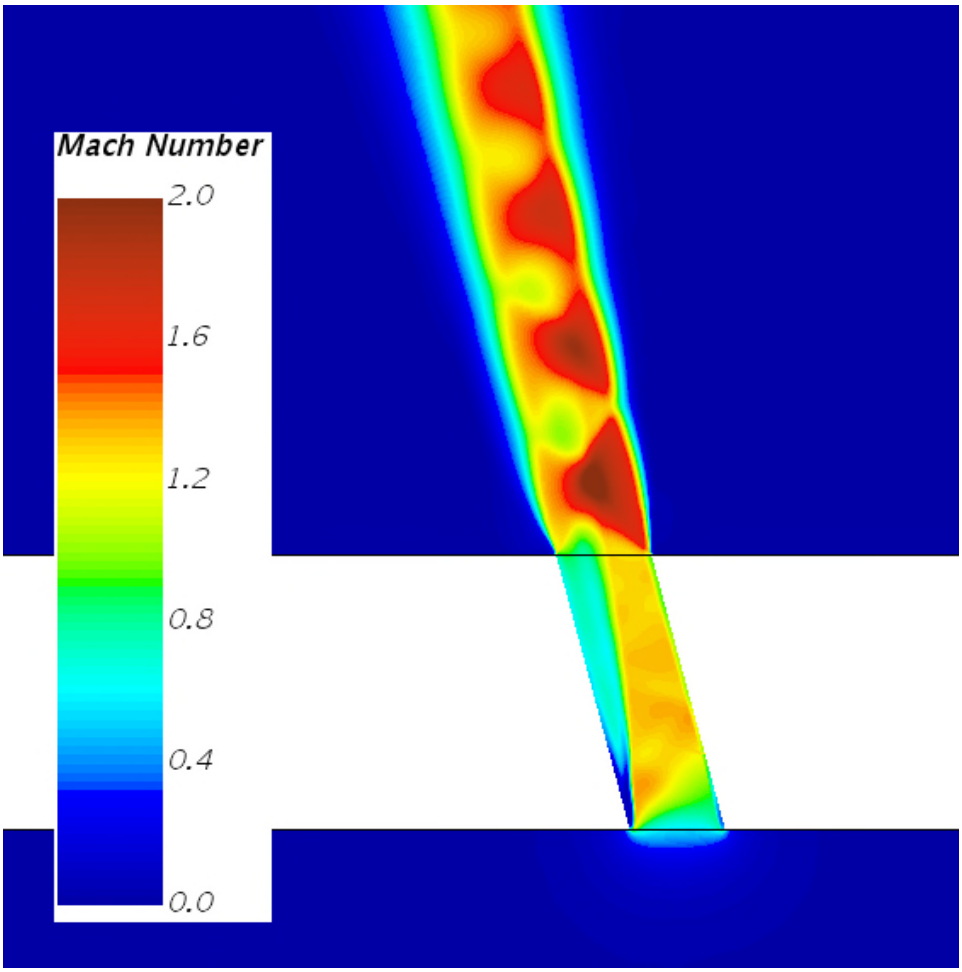

FIGURE 4.3.13 Computational Mach number contours for choked inclined (15°) gas jet (Source: Sheridan et al., 2019).

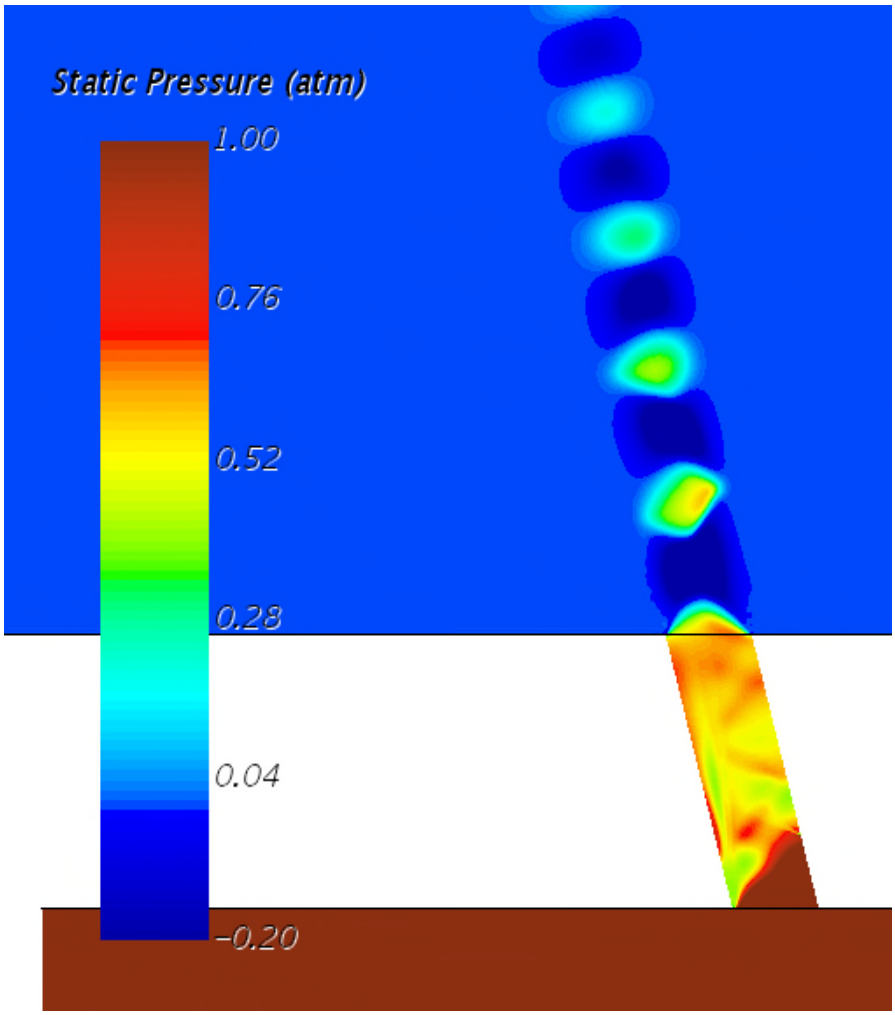

FIGURE 4.3.14 Computational static pressure contours for the choked inclined (15°) gas jet (Source: Sheridan et al., 2019).

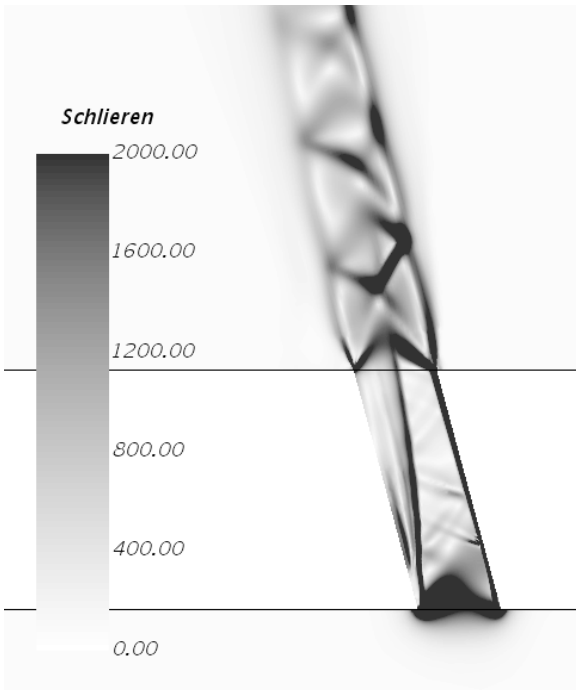

A

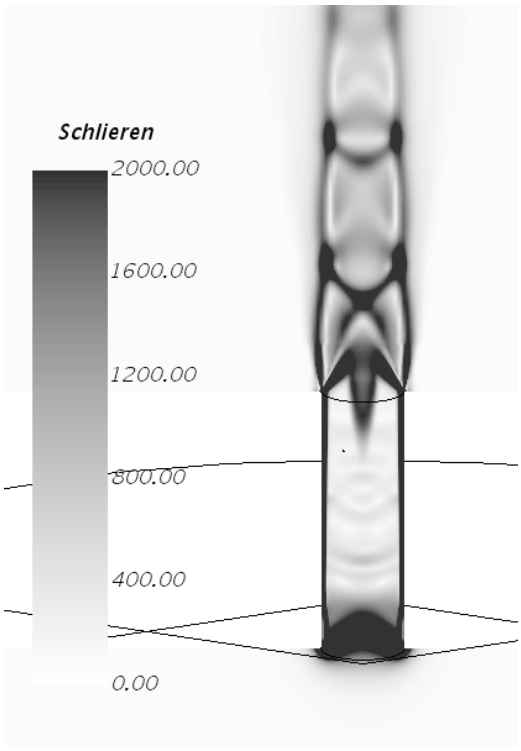

B

FIGURE 4.3.15 Computational density gradient for choked inclined jet at 15° (A) side (injection plane) view (B) front (normal to injection plane) view (Source: Sheridan et al., 2019).

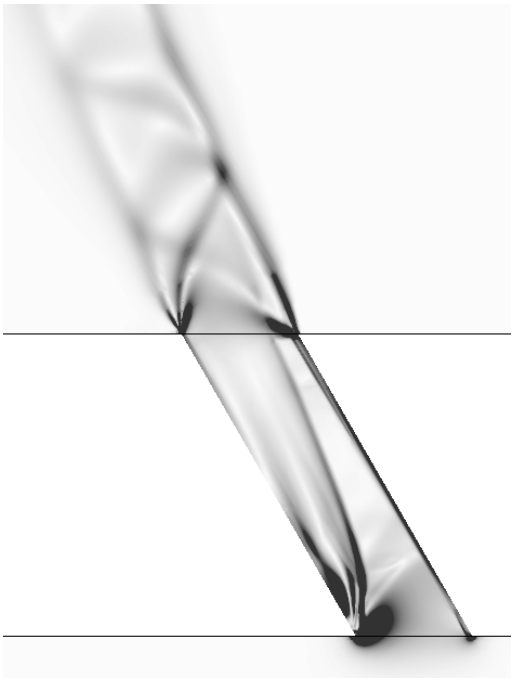

A

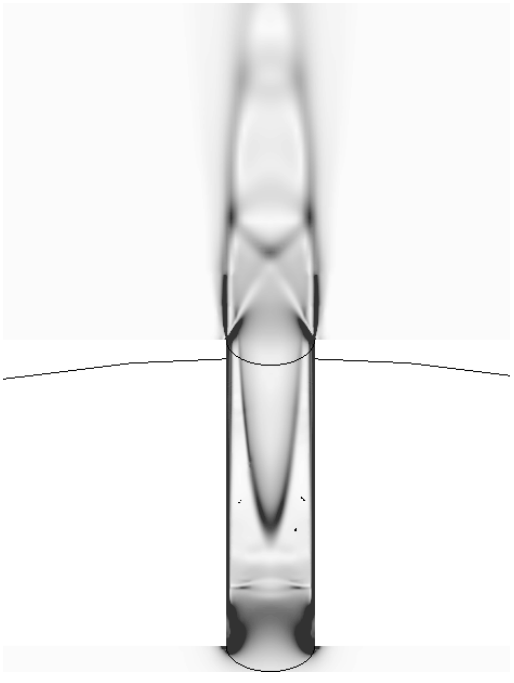

B

FIGURE 4.3.16 Computational density gradient for choked inclined jet at 30° (A) side (injection plane) view (B) front (normal to injection plane) view (Source: Sheridan et al., 2019).

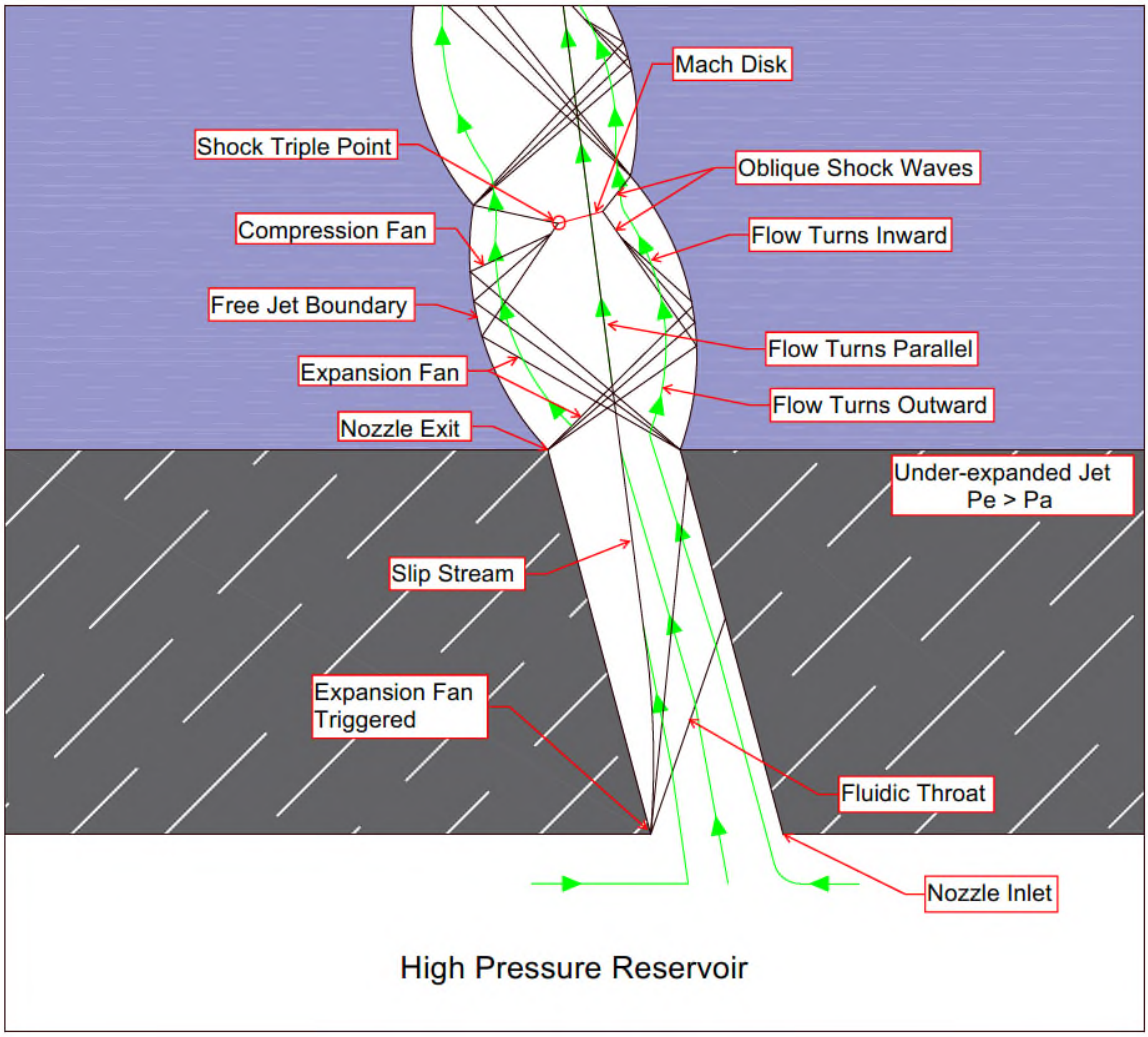

FIGURE 4.3.17 Wave structure of an under-expanded jet with a sharp edge inlet injected at an angle into a quiescent environment. Note that flow at inlet has large direction change on the inward side (left) trigging an expansion fan and generating a fluid throat internal to the nozzle increasing velocity to $M \geq 1$. Flow entering from the outward side (right) of the nozzle inlet does not have a large direction change.

CHAPTER V

CONCLUSIONS

5.1 Summary

Three cylindrical nozzles with different injection angles (normal injection, 15^{o}, and 30^{o}) and 1.59 mm in diameter, were investigated using PIV. The test conditions were limited to choked air injection in still air. The experimental results included the jet ‘s horizontal and vertical velocities as well as the velocity component normal to the injection direction, the entrainment flow velocity, and the vorticity magnitude. A computational study by our collaborators of the same geometry was used to confirm the present findings.

5.2 Conclusions

The major conclusions of the present study are as follows:

1. The flow of a choked jet issuing from an inclined nozzle experiences a lack of symmetry along the injection axis of the jet. This was confirmed by both the present experimental methods and a companion computational study (Sheridan et al, 2019). The flow asymmetry for inclined injection is attributed to the asymmetry of the expansion fans triggering at both the nozzle’s inlet and exit sections.
2. A supersonic flow exit was achieved in the present straight cylindrical nozzle without the use of traditional convergent-divergent (De Laval) nozzle geometry. This was plausible due to the presence of sharp entrance edge that acted as the nozzle throat

3. and triggered the expansion fans necessary to accelerate the flow to supersonic speeds.
4. At the exit section of the inclined nozzle, the expansion fan triggered at the outward edge (right) of the nozzle's exit tended to dominate a larger region of the jet when compared with the fan triggered at the inward edge (left) causing the production of higher flow rates in the outward direction resulting in non-symmetric shock diamond structures.
5. At the inclined nozzle inlet, the flow was dominated by the expansion fan on the opposite edge (left) due to the sharp entrance and the large change in flow direction (i.e. turning) compared to the small turning on the right-hand side where the incoming flow followed the nozzle wall smoothly. This caused most of the flow to be directed (i.e. funneled) toward the outward expansion fan triggered at the nozzle's exit.
6. The inclined nozzle exit was not fully utilized for the exit flux. The flow mainly occupied the right-hand (outward) side of the nozzle whereas the left (inward) side experienced very small velocities. This could result in large error if an inclined nozzle designer did not take this into consideration when calculating the nozzle exit flow for choked conditions.

5.3 Recommendations for Future Work

1. The present study was limited to circular straight injection ports with short length/diameter ratio and sharp entrance. Further studies should focus on the inner flow field for different port geometries including nozzles with long length/diameter ratio and smooth entrance curvature.
2. The present diagnostics were limited to two-dimensional PIV. Although this technique was successful in revealing the structure of the inclined shock diamonds formed outside the port exit, a three-dimensional diagnostics (e.g. Holographic PIV or stereo PIV) would be needed to resolve the essentially three-dimensional entrainment flow.

3. The jet mixing could be qualitatively assessed by observing the spread of the inner seeding particles injected in unseeded environment. The use of planner laser induced fluorescence (PLIF) technique would help to quantify the jet mixing with the ambient.
4. The current study was limited to non-reacting flows. The study should expand to the injection of reacting gas jets (flammable) to investigate the effect of the heat release (chemical combustion) on the jet structure and the ambient entrainment.

REFERENCES

[1] André, B., Thomas, C., Christophe, B. “Investigation of the Mixing Layer of Underexpanded Supersonic Jets by Particle Image Velocimetry.” *International Journal of Heat and Fluid Flow*, vol. 50, 2014, pp. 188–200., doi:10.1016/j.ijheatfluidflow.2014.08.004.

[2] Boxx, I.G., Heinold, O., Geigle, K.P. “Laser-Induced Incandescence Measurements in a Fired Diesel Engine at 3 KHz.” Experiments in Fluids, vol. 56, no. 1, 2015, doi:10.1007/s00348-014-1865-7.

[3] Buttay, R., Lehnasch, G., Mura, A. “Turbulent Mixing and Molecular Transport in Highly under-Expanded Hydrogen Jets.” *International Journal of Hydrogen Energy*, vol. 43, no. 17, 2018, pp. 8488–8505., doi:10.1016/j.ijhydene.2018.03.054.

[4] Chauhan, V., Kumar, A., Rathakrishnan, E. “Mixing Characteristics of Underexpanded Elliptic Sonic Jets from Orifice and Nozzle.” *Journal of Propulsion and Power*, vol. 31, no. 2, 2015, pp. 496–504., doi:10.2514/1.b35451.

[5] Chen, F., Allou, A., Douasbin, Q., Selle, L., Parisse, J.D. “Influence of Straight Nozzle Geometry on the Supersonic under-Expanded Gas Jets.” *Nuclear Engineering and Design*, vol. 339, 2018, pp. 92–104., doi:10.1016/j.nucengdes.2018.09.003.

[6] Douvos, G. “Calculating the Optimum Focus Distance.” OptimumCS-Pro Optical Science, 2014, www.georgedouvos.com/douvos/OptimumCS-Pro_Optical_Science.html.

[7] Franquet, E., Perrier, V., Gibout, S., Bruel, P. “Free Underexpanded Jets in a Quiescent Medium: A Review.” *Progress in Aerospace Sciences*, vol. 77, 2015, pp. 25–53., doi:10.1016/j.paerosci.2015.06.006.

[8] Görtler, H., “Über eine dreidimensionale Instabilität laminarer Grenzchichten an konkaven Wänden” Ges. d. Wiss. Göttingen, Nachr. A. d. Math., Bd. 2, Nr. 1, 1940

[9] Iffa, E.D., Rashid, A., Aziz, A., Malik, A.S. “Velocity Field Measurement of a Round Jet Using Quantitative Schlieren.” *Applied Optics*, vol. 50, no. 5, 2011, p. 618., doi:10.1364/ao.50.000618.

[10] John, J.E.A., and Theo G. Keith. Gas Dynamics. Pearson Prentice Hall, 2006.

[11] Kerhervé, F., Jordan, P., Gervais, Y., Valiere, J.C, Braud, P. “Two-Point Laser Doppler Velocimetry Measurements in a Mach 1.2 Cold Supersonic Jet for Statistical Aeroacoustic Source Model.” Experiments in Fluids, vol. 37, no. 3, 2004, pp. 419–437., doi:10.1007/s00348-004-0815-1.

[12] Koechner, W. Solid-State Laser Engineering. Springer, 2006.

[13] Li, X., Wu, K., Yao, W., Fan, X. “A Comparative Study of Highly Underexpanded Nitrogen and Hydrogen Jets Using Large Eddy Simulation.” *International Journal of Hydrogen Energy*, vol. 41, no. 9, 2016, pp. 5151–5161., doi:10.1016/j.ijhydene.2016.01.120.

[14] Li, X., Fan, E., Yao, W., Fan, X. “Numerical Investigation of Characteristic Frequency Excited Highly Underexpanded Jets.” *Aerospace Science and Technology*, vol. 63, 2017, pp. 304–316., doi:10.1016/j.ast.2017.01.005.

[15] Liu, Q., Baccarella, D., McGann, B., Lee, T. “Experimental Investigation of Single Jet and Dual Jet Injection in a Supersonic Combustor.” 2018 AIAA Aerospace Sciences Meeting, 2018, doi:10.2514/6.2018-1363.

[16] Matsuo, S., Tanaka, M., Otobe, Y., Kashimura, H., Kim, H.D., Setoguchi, T. “Effect of Axisymmetric Sonic Nozzle Geometry on Characteristics of Supersonic Air Jet.” *Journal of Thermal Science*, vol. 13, no. 2, 2004, pp. 121–126., doi:10.1007/s11630-004-0019-2.

[17] Meier, A.H., and Thomas R. “Imaging Laser Doppler Velocimetry.” Experiments in Fluids, vol. 52, no. 4, 2011, pp. 1017–1026., doi:10.1007/s00348-011-1192-1.

[18] Otobe, Y., Kahimura, H., Matsuo, S., Setoguchi, T., Kim, H.D. “Influence of Nozzle Geometry on the near-Field Structure of a Highly Underexpanded Sonic Jet.” *Journal of Fluids and Structures*, vol. 24, no. 2, 2008, pp. 281–293., doi:10.1016/j.jfluidstructs.2007.07.003.

[19] Panda, J., and Seasholtz, R.G. “Measurement of Shock Structure and Shock–Vortex Interaction in Underexpanded Jets Using Rayleigh Scattering.” Physics of Fluids, vol. 11, no. 12, 1999, pp. 3761–3777., doi:10.1063/1.870247.

[20] Ruggles, A.J., and Ekoto, I.W. “Ignitability and Mixing of Underexpanded Hydrogen Jets.” *International Journal of Hydrogen Energy*, vol. 37, no. 22, 2012, pp. 17549–17560., doi:10.1016/j.ijhydene.2012.03.063.

[21] Ruggles, A.J., and Ekoto, I.W. “Experimental Investigation of Nozzle Aspect Ratio Effects on Underexpanded Hydrogen Jet Release Characteristics.” *International Journal of Hydrogen Energy*, vol. 39, no. 35, 2014, pp. 20331–20338., doi:10.1016/j.ijhydene.2014.04.143.

[22] Seasholtz, R., Panda, J., Elam, K.A. “Rayleigh Scattering Diagnostic for Dynamic Measurement of Velocity Fluctuations in High Speed Jets.” 39th Aerospace Sciences Meeting and Exhibit, 2001, doi:10.2514/6.2001-847.

[23] Settles, G.S., Krause, E., Futterer, H. “Theodor Meyer—Lost Pioneer of Gas Dynamics.” *Progress in Aerospace Sciences*, vol. 45, no. 6-8, 2009, pp. 203–210., doi:10.1016/j.paerosci.2009.06.001.

[24] Sheridan A.M., Srivastava, S., Henneke, M., Raza, M.S., Sallam, K.A. “Inclined Injection of Under Expanded Supersonic Gas Jet.” International Mechanical Engineering Congress and Exposition, 2019, IMECE2019-12020.

[25] Slabaugh, C.D., Pratt, A., Lucht, R.P. “Simultaneous 5 KHz OH-PLIF/PIV for the Study of Turbulent Combustion at Engine Conditions.” Applied Physics B, vol. 118, no. 1, 2014, pp. 109–130., doi:10.1007/s00340-014-5960-5.

[26] Thielicke, W. (2014). The flapping flight of birds: Analysis and application. [S.l.]: [S.n.].

[27] Thielicke, W. PIVlab - particle image velocimetry (PIV) tool (https://www.mathworks .com/matlabcentral/fileexchange/27659-pivlab-particle-image-velocimetry-piv-tool), MATLAB Central File Exchange. Retrieved July 12, 2019.

[28] Venkatakrishnan, L. “Density Measurements in an Axisymmetric Underexpanded Jet Using Background Oriented Schlieren Technique.” 24th AIAA Aerodynamic Measurement Technology and Ground Testing Conference, 2004, doi:10.2514/6.2004-2603.

[29] Zagidullin, M.V., Torbin, A.P., Chernyshov, A.A., Heaven, M.C.m Azyazov, V.N. “Gas Flow Visualization Using Laser-Induced Fluorescence.” Procedia Engineering, vol. 106, 2015, pp. 92–96., doi:10.1016/j.proeng.2015.06.012.

[30] Zapryagaev, V., Kiselev, N., Gubanov, D. “Shock-Wave Structure of Supersonic Jet Flows.” *Aerospace*, vol. 5, no. 2, 2018, p. 60., doi:10.3390/aerospace5020060.

APPENDICES

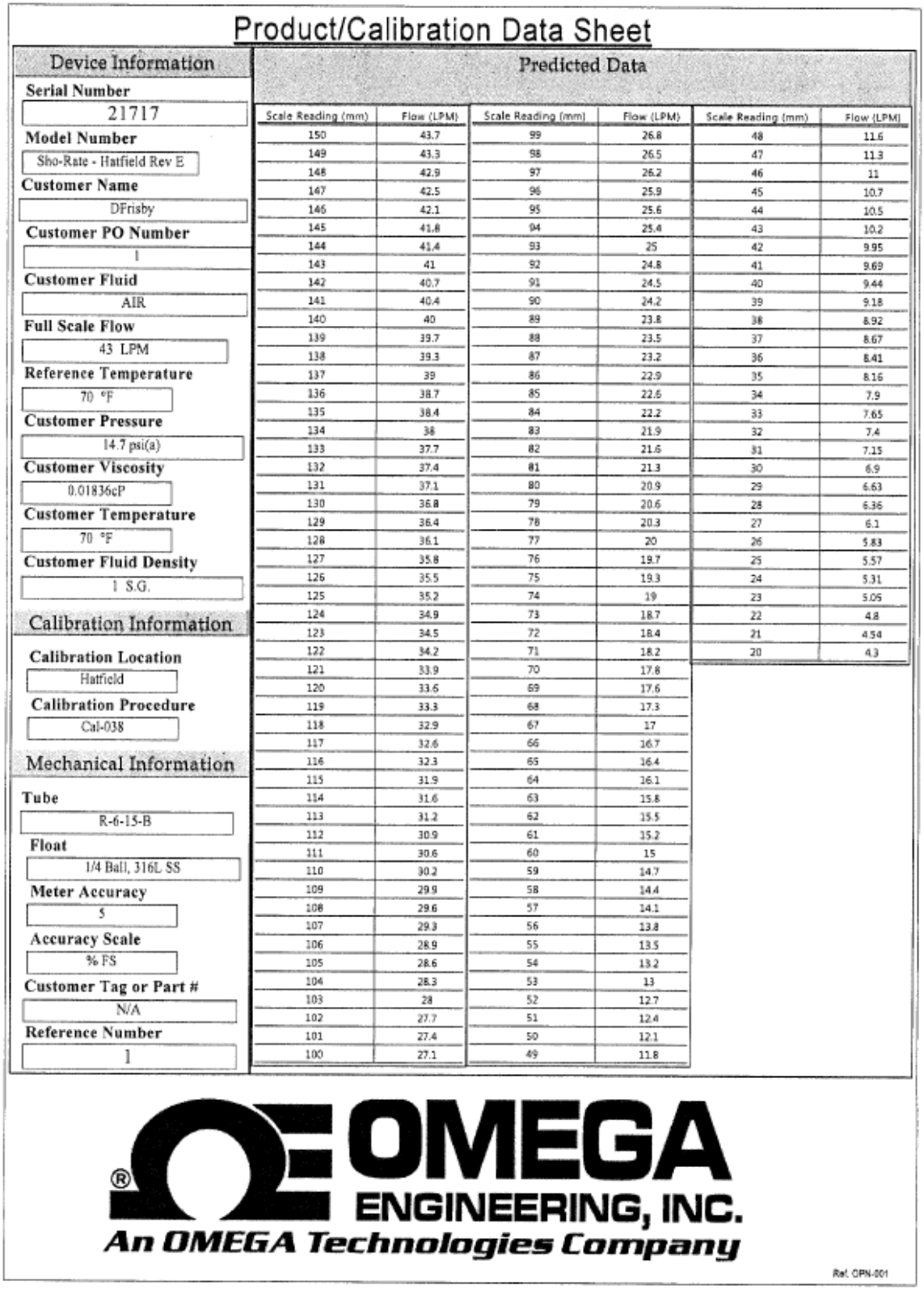

Product/Calibration Data Sheet

Device Information

Serial Number
21717

Model Number
Sho-Rate - Hatfield Rev E

Customer Name
DFrisby

Customer PO Number
1

Customer Fluid
AIR

Full Scale Flow
43 LPM

Reference Temperature
70 °F

Customer Pressure
14.7 psi(a)

Customer Viscosity
0.01836cP

Customer Temperature
70 °F

Customer Fluid Density
1 S.G.

Calibration Information

Calibration Location
Hatfield

Calibration Procedure
Cal-038

Mechanical Information

Tube
R-6-15-B

Float
1/4 Ball, 316L SS

Meter Accuracy
5

Accuracy Scale
% FS

Customer Tag or Part #
N/A

Reference Number
1

Predicted Data

Scale Reading (mm)	Flow (LPM)	Scale Reading (mm)	Flow (LPM)	Scale Reading (mm)	Flow (LPM)
150	43.7	99	26.8	48	11.6
149	43.3	98	26.5	47	11.3
148	42.9	97	26.2	46	11
147	42.5	96	25.9	45	10.7
146	42.1	95	25.6	44	10.5
145	41.8	94	25.4	43	10.2
144	41.4	93	25	42	9.95
143	41	92	24.8	41	9.69
142	40.7	91	24.5	40	9.44
141	40.4	90	24.2	39	9.18
140	40	89	23.8	38	8.92
139	39.7	88	23.5	37	8.67
138	39.3	87	23.2	36	8.41
137	39	86	22.9	35	8.16
136	38.7	85	22.6	34	7.9
135	38.4	84	22.2	33	7.65
134	38	83	21.9	32	7.4
133	37.7	82	21.6	31	7.15
132	37.4	81	21.3	30	6.9
131	37.1	80	20.9	29	6.63
130	36.8	79	20.6	28	6.36
129	36.4	78	20.3	27	6.1
128	36.1	77	20	26	5.83
127	35.8	76	19.7	25	5.57
126	35.5	75	19.3	24	5.31
125	35.2	74	19	23	5.05
124	34.9	73	18.7	22	4.8
123	34.5	72	18.4	21	4.54
122	34.2	71	18.2	20	4.3
121	33.9	70	17.8		
120	33.6	69	17.6		
119	33.3	68	17.3		
118	32.9	67	17		
117	32.6	66	16.7		
116	32.3	65	16.4		
115	31.9	64	16.1		
114	31.6	63	15.8		
113	31.2	62	15.5		
112	30.9	61	15.2		
111	30.6	60	15		
110	30.2	59	14.7		
109	29.9	58	14.4		
108	29.6	57	14.1		
107	29.3	56	13.8		
106	28.9	55	13.5		
105	28.6	54	13.2		
104	28.3	53	13		
103	28	52	12.7		
102	27.7	51	12.4		
101	27.4	50	12.1		
100	27.1	49	11.8		

OMEGA®
ENGINEERING, INC.
An OMEGA Technologies Company

Ref. OPN-001

FIGURE A.1.1 Omega correlation chart for FL-1448-S series tube

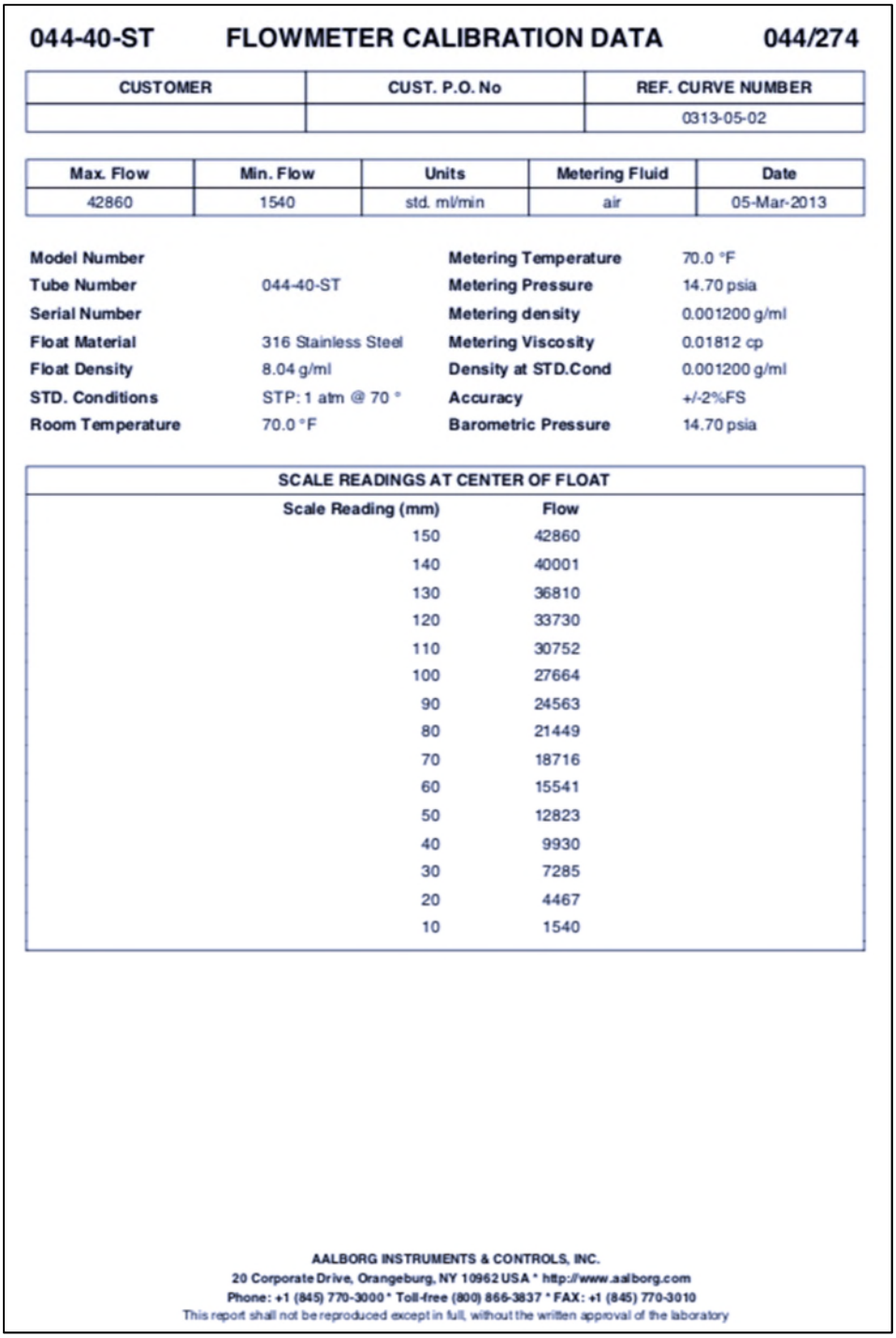

044-40-ST FLOWMETER CALIBRATION DATA 044/274

CUSTOMER	CUST. P.O. No	REF. CURVE NUMBER
		0313-05-02

Max. Flow	Min. Flow	Units	Metering Fluid	Date
42860	1540	std. ml/min	air	05-Mar-2013

Model Number		**Metering Temperature**	70.0 °F
Tube Number	044-40-ST	**Metering Pressure**	14.70 psia
Serial Number		**Metering density**	0.001200 g/ml
Float Material	316 Stainless Steel	**Metering Viscosity**	0.01812 cp
Float Density	8.04 g/ml	**Density at STD.Cond**	0.001200 g/ml
STD. Conditions	STP: 1 atm @ 70 °	**Accuracy**	+/-2%FS
Room Temperature	70.0 °F	**Barometric Pressure**	14.70 psia

SCALE READINGS AT CENTER OF FLOAT

Scale Reading (mm)	Flow
150	42860
140	40001
130	36810
120	33730
110	30752
100	27664
90	24563
80	21449
70	18716
60	15541
50	12823
40	9930
30	7285
20	4467
10	1540

AALBORG INSTRUMENTS & CONTROLS, INC.
20 Corporate Drive, Orangeburg, NY 10962 USA * http://www.aalborg.com
Phone: +1 (845) 770-3000 * Toll-free (800) 866-3837 * FAX: +1 (845) 770-3010

FIGURE A.1.2 Omega correlation chart for 044-40-ST tube

It was necessary to confirm that the rotameters used in the experimental setup were appropriately sized to achieve the desired flow rate through the orifice required to achieve choked flow conditions. The Crane equation 6-32 ["Flow of Fluids Through Valves, Fittings, and Pipe", Technical Paper No. 410, 2018, Crane Co.] was used to calculate the theoretical volumetric flow rate being relieved through the test orifices.

$$Q = Y * C * A_o * \sqrt{\frac{2g*144*\Delta P}{\rho}} \quad (4.2b.1)$$

where Y is the expansion factor that must be included for the flow of compressible fluids and can be obtained from Fig. A.2 (source: Crane's technical paper TP-410, 2018). The expansion factor is a function of the specific heat ratio (k) the ratio of orifice diameter to inlet diameter, and the ratio between the absolute downstream to upstream pressures. While 'C' represents the flow coefficient for the orifice (Figure A.3) and eliminates the need to calculate the velocity of approach (*0.82 for a nozzle with an L/D of 3*) [Sheridan et al., 2019] and ρ is the gas density. At a chamber pressure of 27.8 psia the density of the air is ~0.13 lbm/ft^3. Using equation 4.2b.1, it was calculated that a theoretical volumetric flow rate through the test orifice at a at a chamber pressure of 27.8 psia would be approximately 66.4 SCFH (31.34 L/m).

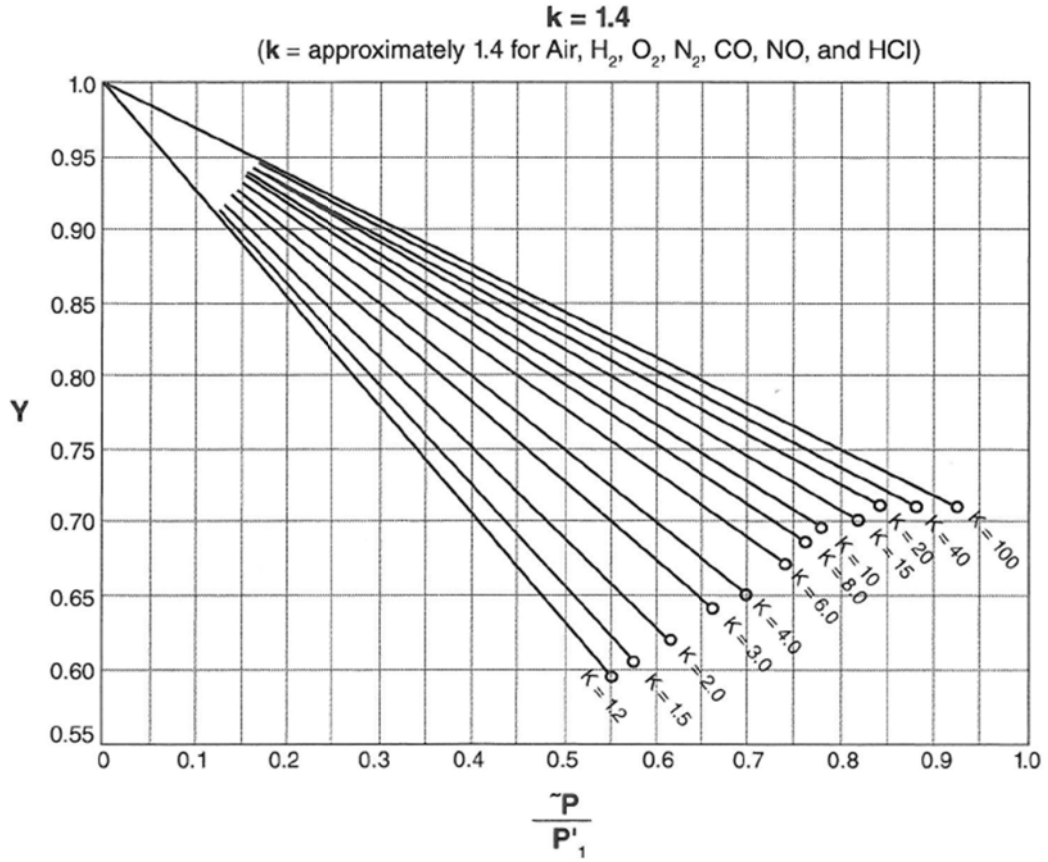

Limiting Factors For Sonic Velocity
k = 1.4

K	$\frac{\Delta P}{P'_1}$	Y
1.2	.552	.588
1.5	.576	.606
2	.612	.622
3	.662	.639
4	.697	.649
6	.737	.671
8	.762	.685
10	.784	.695
15	.818	.702
20	.839	.710
40	.883	.710
100	.926	.710

FIGURE A.2 Expansion Factor, Y (Source: "Flow of Fluids Through Valves, Fittings, and Pipe", Technical Paper No. 410, 1999, Crane Co.).

Flow Coefficient C for Square Edge Orifices and Nozzles[27]

$$C = \frac{C_d}{\sqrt{1-\beta^4}}$$

$$K_{orifice} = \left[\frac{\sqrt{1-\beta^4\left(1-{C_d}^2\right)}}{C_d\beta^2} - 1\right]^2$$

$$\beta = \frac{d_1}{d_2}$$

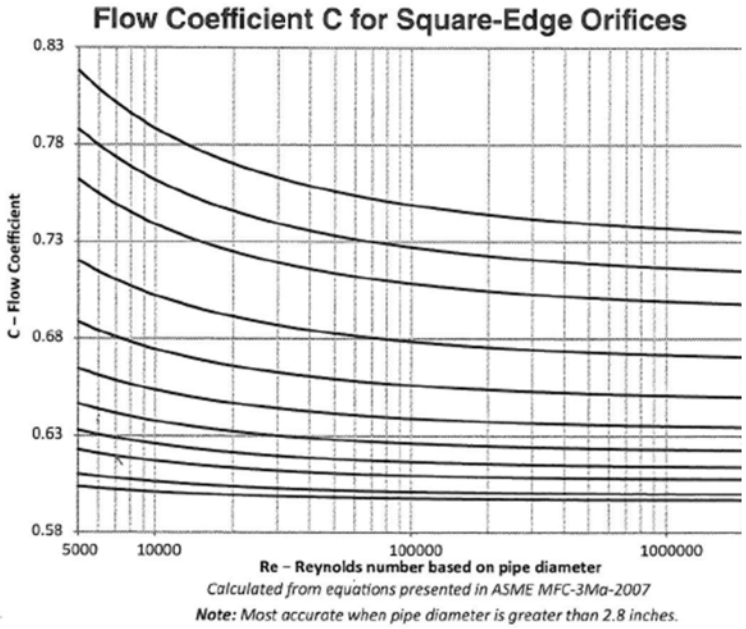

FIGURE A.3 Flow Coefficient for square edged orifice (Source: "Flow of Fluids Through Valves, Fittings, and Pipe", Technical Paper No. 410, 1999, Crane Co.).

VITA

Alex Michael Sheridan

Candidate for the Degree of

Master of Science

Thesis: EFFECTS OF INJECTION ANGLE ON SONIC GASEOUS JETS

Major Field: Mechanical & Aerospace Engineering

Biographical:

Education:

Completed the requirements for the Master of Science in Mechanical Engineering at Oklahoma State University, Stillwater, Oklahoma in July 2019.

Completed the requirements for the Bachelor of Science in Mechanical Engineering at Oklahoma State University, Stillwater, Oklahoma in December 2012.

Experience:

Worked as an engineering apprentice for Express Integrated Technologies from May 2008 to July 2012. Worked as an Engineering Project Manager II for John Zink Company, LLC from July 2012 to December 2015. Currently work as an Instrumentation and Controls Engineer III for John Zink Company, LLC since June 2015.